Chemical Geology 357 (2013) 117–133

Contents lists available at ScienceDirect

Chemical Geology

journal homepage: www.elsevier.com/locate/chemgeo

Trace element behavior during serpentinization/de-serpentinization of an eclogitized oceanic lithosphere: A LA-ICPMS study of the Lanzo ultramafic massif (Western Alps)

Baptiste Debret [a,b,c,*], Muriel Andreani [d], Marguerite Godard [e], Christian Nicollet [a,b,c], Stéphane Schwartz [f], Romain Lafay [f]

[a] Clermont Université, Université Blaise Pascal, Laboratoire Magmas et Volcans, Clermont-Ferrand, France
[b] CNRS, UMR6524, LMV, Clermont-Ferrand, France
[c] IRD, R163, LMV, Clermont-Ferrand, France
[d] Laboratoire de Géologie de Lyon, ENS — Université Lyon 1, Villeurbanne, France
[e] Géosciences Montpellier, Université Montpellier 2, Montpellier, France
[f] Institut des Sciences de la Terre, Université Grenoble I, Grenoble, France

ARTICLE INFO

Article history:
Received 20 November 2012
Received in revised form 7 August 2013
Accepted 13 August 2013
Available online 20 August 2013

Editor: D.B. Dingwell

Keywords:
Lizardite
Antigorite
Trace element
Oceanic lithosphere
Subduction

ABSTRACT

Serpentinites are one of the major components of the oceanic lithosphere and are stable in the slab and the mantle wedge up to 100–150 km depth in subduction zones. During oceanic mantle hydration and alteration, they trap trace and fluid mobile (FME: B, Li, As, Sb, Rb, Ba, Cs, Sr, U and Pb) elements that participate to elemental transfer occurring between the dehydrating slab and the mantle wedge in subduction context. The Lanzo massif is an eclogitized oceanic lithosphere that preserved its oceanic structure and recorded different steps of serpentinization/de-serpentinization from oceanic lizardite to prograde antigorite in subduction context, up to its dehydration and secondary olivine crystallization, and finally retrograde antigorite during massif exhumation. It constitutes a suitable place to study trace element behavior during serpentinization/de-serpentinization processes and associated chemical transfers between the different envelopes of the oceanic lithosphere and the mantle wedge.

Geochemical analyses of serpentine and associated minerals show that the serpentinization/de-serpentinization of the Lanzo massif took place in a relatively closed system without significant trace element transfer between the different parts of the oceanic lithosphere. In the deeper part of the lithosphere, from the slightly serpentinized mantle peridotites (SSP, <20% serpentinization) to the paleo-Moho, composed of massive serpentinites (MS, 80% serpentinization), the trace elements mobility is reduced. The chemical composition of lizardite and antigorite is homogenized with the local degree of serpentinization: in SSP, serpentine veins composition is inherited from the host mineral while, in MS, their composition is homogenous between destabilized phases at the scale of the outcrop (~5 m). In the shallowest part of the oceanic lithosphere, from the paleo-Moho to the oceanic paleo-seafloor, the serpentinites are foliated (FS, >90% serpentinization). In that zone, the alpine deformation enhances the mobility of trace elements and permits their redistribution and the homogenization of antigorite composition at massif scale. Locally, in the SSP and MS, the crystallization of metamorphic veins of ~1–2 m corresponds to channelized fluid flows that allowed fluid transfers – and thereby trace elements – to longer distance.

The successive crystallizations of antigorite and then olivine are accompanied by a diminution of some FME (B, Li, As, Sb, Ba, Rb) and Eu contents attesting that these elements are removed from slab to mantle wedge during subduction.

1. Introduction

Subduction represents one of the major processes of mass transfer on Earth. Serpentinites contain up to 13% H_2O and represent a large and essential reservoir of fluids and trace elements in subduction zone (Hattori and Guillot, 2007). The dehydration of the upper part of the subducted slab (oceanic sediments and altered peridotites and gabbros), down to 130–160 km (Wunder and Schreyer, 1997), is responsible for the fluid and element transfers to the mantle wedge. It conducts to modify the composition of metasomatized mantle wedge peridotites and thus that of arc magmas.

Mantle peridotites are widely exposed on the seafloor of slow and ultra-slow spreading ridges, where they are a major feature of these magma poor settings (Cannat et al., 1995; Dick et al., 2003). In the

* Corresponding author at: Clermont Université, Université Blaise Pascal, Laboratoire Magmas et Volcans, Clermont-Ferrand, France.
E-mail address: b.debret@opgc.univ-bpclermont.fr (B. Debret).

0009-2541/$ – see front matter © 2013 Elsevier B.V. All rights reserved.
http://dx.doi.org/10.1016/j.chemgeo.2013.08.025

first 3 to 6 km, they are highly serpentinized into lizardite and chrysotile as a result of seawater circulation (Canales et al., 2000; Mével, 2003; Andreani et al., 2007). Recent results revealed that the oceanic serpentinization causes an enrichment of peridotite in trace elements, in particular fluid mobile elements (FME: B, Li, As, Sb, Rb, Ba, Cs, Sr, U and Pb) and, in the most altered samples, in light rare earth elements (LREE; Paulick et al., 2006; Vils et al., 2008; Andreani et al., 2009; Morishita et al., 2009; Kodolanyi et al., 2012). The serpentinites are a vector of trace element transfer through subduction zones until their dehydration around 150 km (Wunder and Schreyer, 1997). The subduction of the oceanic lithosphere causes first the transformation of lizardite and chrysotile into antigorite and then of antigorite into olivine +/− orthopyroxene +/− chlorite by dehydration (Evans, 2004; Scambelluri et al., 2004; Padron-Navarta et al., 2010). The chemical composition of the fluid released during these reactions is determinant for both estimating elemental transfers between subducted slab and the mantle wedge and better understanding other processes like arc magma production at depth. This composition has been evaluated in several studies using different approaches. Some authors assess the chemical composition of fluid released by the slab by comparing the composition of oceanic serpentinites with mantle wedge serpentinites. They proposed that the mantle wedge is highly contaminated by B, Li, Cs, Cl, Sr, As and Sb-rich fluids (Savov et al., 2005, 2007; Deschamps et al., 2010, 2011; Kodolanyi and Pettke, 2011). However, those studies do not directly estimate the transfers associated with the different dehydration serpentine reactions along the subduction history of the slab down to its dehydration. Vils et al. (2011) completed those observations by measuring the composition in Be, Li and B of serpentine from several alpine ophiolites recording different metamorphic conditions during the lizardite to antigorite transition. They observed large losses of Li and B during the lizardite to antigorite transition but, a quantitative assessment of light element loss was limited because those different serpentine units had different initial chemical composition and have undergone different reaction pathways. Scambelluri et al. (2001, 2004) also tried to assess the composition of fluid released by the slab at shallower depth during the antigorite dehydration. They presented trace element analyses of fluid inclusion trapped in secondary olivine and orthopyroxene, interpreted as representative of the fluid released during antigorite break down. Those are enriched in Rb, Sr, Cs, Pb, Li, B and alkalis and are depleted in HFSE. Garrido et al. (2005) confirmed, by studying dehydrated assemblages, that serpentine dehydration is a source of fluid leaching large ion lithophile element (LILE), Pb and Sr from the slab to the mantle wedge.

The trace element composition of fluid released by serpentine transition phases, from lizardite breakdown to antigorite and then olivine, is commonly estimated by referring to several massifs that recorded different (de-)serpentinization steps (e.g. see references above). The Lanzo massif is, to our knowledge, the only oceanic lithosphere where the different metamorphic stages have been preserved form oceanic hydration to subduction dehydration (Groppo and Compagnoni, 2007; Debret et al., 2013). Furthermore, its oceanic structure has been preserved during subduction. Hence, it constitutes a unique opportunity to follow, during subduction, the different metamorphic reactions and their associated element transfer occurring in an oceanic lithosphere. We present a systematic chemical study of serpentinite in bulk rock and of their forming minerals (primary mantle minerals, the oceanic lizardite, the prograde antigorite, the dehydrated assemblages and the retrograde antigorite).

2. Geological setting and petrological background

The Lanzo massif is an ultramafic eclogitized body located 30 km at the North-Western of Torino (Italy). To the west, the massif is bordered by meta-ophiolites and the Schistes Lustrés unit, to the south and east it is bounded by sediments of Po plain and to the north by the high pressure continental unit of Sesia. The entire massif is dominated by plagioclase peridotites surrounded by an envelope of serpentinites (Boudier, 1978; Müntener et al., 2005). Earlier structural, petrographic and geochemical studies have shown that the massif is composed of fertile lherzolitic peridotites impregnated by asthenospheric melts during the massif exhumation in an ocean–continent transition context (OCT, Nicolas et al., 1972; Bodinier, 1988; Piccardo et al., 2007a, 2007b; Kaczmarek and Müntener, 2008). We focus our study in the northern part of the massif where the oceanic structure is preserved (Lagabrielle et al., 1989; Pelletier and Müntener, 2006; Debret et al., 2013). The oceanic paleo-seafloor is marked by the presence of oceanic meta-basaltes, meta-quartzite associated with metasediments, and meta-ophicarbonates bordering locally an ultramafic unit (Fig. 1). This unit is made of 3 compartments: the center is composed of slightly serpentinized peridotites (SSP, ≤20% serpentinization), it is surrounded by a thin zone of massive serpentinites (MS, ~80% serpentinization) and then by an envelope of foliated serpentinites (FS, fully serpentinized) of 3–5 km large. The contact between the MS and the SSP corresponds to a paleo-Moho (Fig. 1; Debret et al., 2013). The different lithologies composing the massif record different steps of serpentinization from oceanic hydration to subduction dehydration at a metamorphism peak estimated in eclogitized metagabbros at 2–2.5 GPa and 550–620 °C (Pelletier and Müntener, 2006).

The SSP were refertilized in OCT context by percolation and impregnation by MOR-type melts (Müntener et al., 2005; Piccardo et al., 2007a). They consist mostly of spinel or plagioclase lherzolites with minor pyroxenites, harzburgite and dunite (Boudier, 1978; Bodinier, 1988; Piccardo et al., 2007a, 2007b; Kaczmarek and Müntener, 2010). The petrographic evolution of ultramafic rocks from Lanzo massif has already been investigated in a previous study (Debret et al., 2013). Three stages of serpentinization have been reported. The SSP preserves an oceanic step of serpentinization marked by lizardite vein crystallization, the low pressure polymorph of the serpentine (Agrinier and Cannat, 1997; Bach et al., 2004), crossing the orthopyroxene and the olivine (Fig. 2a). Those veins display a planar wall and a string of magnetite in their centers. When the hydration is more important, the slightly serpentinized peridotites are divided by a network of serpentinized channels with a width of up to 2 mm. In these channels, the lizardite crystallizes as mesh or bastite texture replacing the olivine and the orthopyroxene (Fig. 2b). Mesh textures consist of a gray homogenous area of serpentine with undulatory extinction delimited by rims with a fibrous aspect and a fine string of magnetite. Bastite textures consist of white serpentine lamellae oriented parallel to the original cleavages of the pyroxene. The clinopyroxene is poorly affected by the oceanic serpentinization.

During the subduction, the lizardite is destabilized into antigorite, the high-temperature/high-pressure (HT/HP) polymorph of the serpentine (Bromiley and Pawley, 2003). This serpentine phase change can be written as: Liz + Bru → Atg (Evans, 2004) or Liz → Atg + MgO + H_2O (Vils et al., 2011) or Liz + SiO_2 → Atg + H_2O (Schwartz et al., 2013). In SSP, this episode is recorded by the crystallization of antigorite veins crossing the clinopyroxene, the orthopyroxene and the olivine. The formation of antigorite has been observed at the expense of the lizardite veins, meshes and bastites (Fig. 2a), confirming that its crystallization postdates the oceanic stage. In MS, the prograde antigorite crystallizes at the expense of the lizardite and the relics of primary minerals of the peridotite. It crystallizes as homogenous area of >100 μm.

At P/T peak, the antigorite breaks down to secondary olivine. In the SSP, this episode is marked by the crystallization of a secondary olivine, as minute grains of ~50 μm, in the center of antigorite veins, replacing the magnetite and the antigorite. In the MS, it is marked by de-serpentinized pseudomorphs of mesh texture: the mesh core is replaced by antigorite and the mesh rims by minute grains of secondary olivine (Fig. 2c).

During the exhumation, in the MS and FS, the previous textures are, respectively, partially to fully obliterated by the crystallization of a retrograde antigorite and chlorite (Fig. 2d). The growth of chlorite is

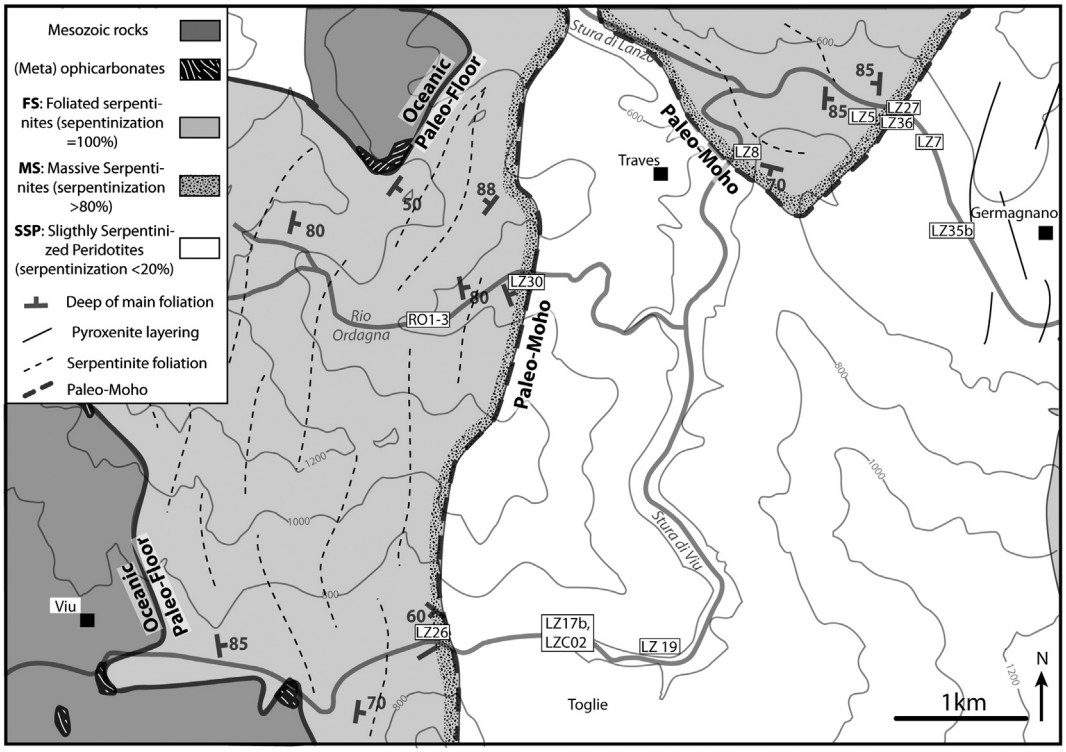

Fig. 1. Geological map of the studied area of Lanzo massif (modified after Pelletier and Müntener, 2006). LZXX: samples localization.

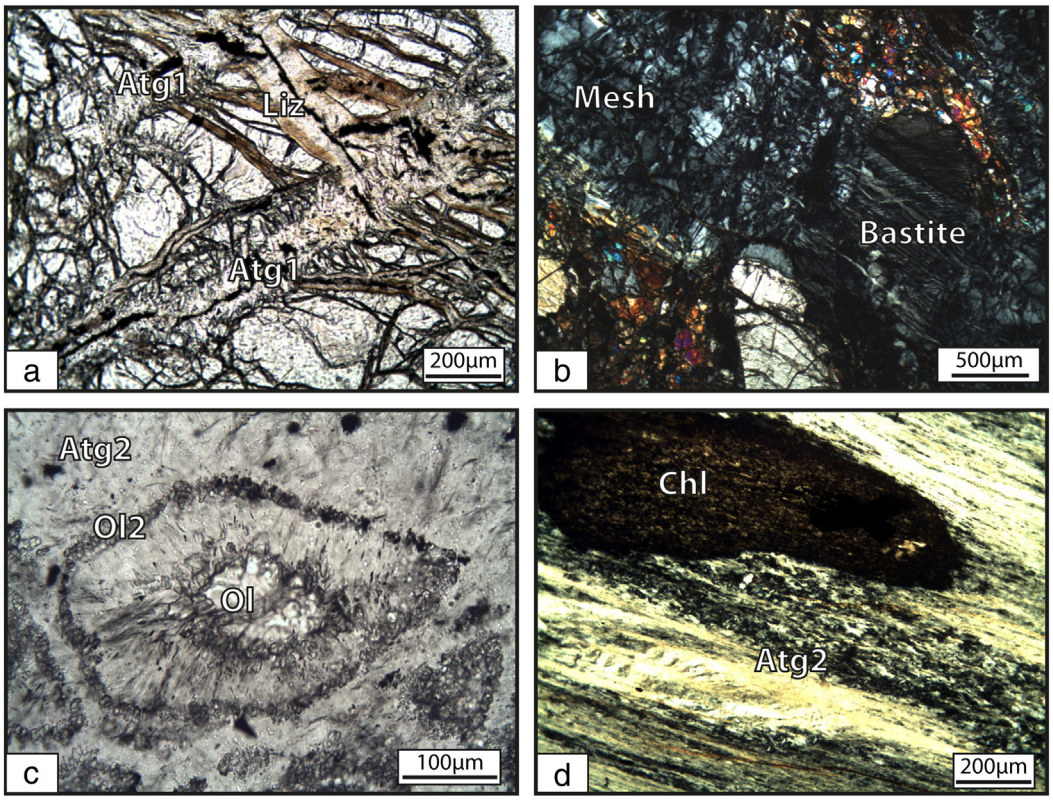

Fig. 2. (a) Microphotograph (plane polarized light) of a SSP. Prograde antigorite veins (Atg1) cross lizardite veins (Liz) and olivine. (b) Microphotograph (cross polarized light) of an oceanic serpentinized channel crossing the SSP. The channel is composed of serpentinite in mesh or bastite texture. (c) Microphotograph (plane polarized light) of an eclogitized mesh like texture in a MS (sample LZ27a): the centre is composed of mantle olivine (Ol) partially destabilized in antigorite and the rims consist of minute secondary olivine (Ol2) associated with antigorite lamellas. (d) Microphotograph (cross polarized light) of a FS. The retrograde antigorite (Atg2) mark the foliation of the rock. Mineral abbreviations are from Whitney and Evans (2010).

associated to spinel destabilization into chromite, magnetite and chlorite. The crystallization of retrograde antigorite is associated to a high alpine deformation stage. Locally, their crystallization has been observed at the expense of secondary olivine.

Locally, a network of metamorphic veins composed of antigorite, secondary olivine +/− chlorite, with a width of several cm, crosses the SSP (Fig. 3a) and the MS (Fig. 3b). Those veins are described in detail by Debret et al. (2013), however for clarity some major characteristics will be introduced here briefly. Those veins are zoned (Fig. 3c–d), their center is composed of secondary olivine associated with prograde antigorite or chlorite and their rims display retrograde antigorite. The secondary olivine crystallized at the expense of prograde serpentine or chlorite and the retrograde antigorite crystallized on the prograde assemblages. The host rock is poorly de-serpentinized and displays similar textures as describe previously (e.g. Fig. 2e).

3. Analytical procedures

3.1. Whole rock analyses

To study the compositional variations during serpentinization processes and the element transfers between the slab and the mantle wedge, we analyzed 14 samples of the different lithologies composing the massif. Four samples of SSP and nine samples of serpentinite (MS and FS) were selected through the serpentinization front (Fig. 1). Sample modal, major and trace element compositions are reported in Tables 1 and 2.

All samples were cut away from weathered surface, pen marks and sticker residues. They were crushed with an anvil and a hammer and powdered in an agate ring-mill.

Whole rock glasses for major elements were prepared with 100 mg of sample powder and with the addition of 300 mg of Li-Metaborate (dilution coefficient of 2000). Major element concentrations were determined by ICP-AES at the Laboratoire Magmas et Volcans of Clermont-Ferrand (France). Concentrations were calibrated against the DR-N basaltic glass standard using the values given in Govindaraju (1994). Precision on samples were determined on repeated analyses of reference basalt BHVO. This typically resulted in a <1% precision for all the measured elements.

Trace element concentrations (Li, Sc, Ti, V, Co, Ni, Cu, Zn, As, Rb, Sr, Y, Zr, Nb, Mo, Cd, Sb, Cs, Ba, Rare Earth Elements (REE), Hf, Ta, W, Pb, Th, and U) were determined at Géosciences Montpellier (University Montpellier 2, France) using an Agilent 7700× quadrupole ICP-MS. 100 mg of powdered samples and 50 mg of powdered standards were prepared following the $HF/HClO_4$ procedure described in Ionov et al. (1992) and Godard et al. (2000). The samples were analyzed after a dilution in $2\%HNO_3$ of 1000 for the trace element depleted serpentinites and peridotites and reference peridotite JP1, and of 2000, 4000 and 8000 respectively for the increasingly trace element enriched reference rock materials UBN, BIR and BEN. Element concentrations were measured by external calibration, except for Nb and Ta that are calibrated by using Zr and Hf, respectively, as internal standards. This technique is an adaptation to ICP-MS analysis of the method described by Jochum et al. (1990) and aims at avoiding memory effects due to the introduction of concentrated Nb–Ta solutions in the instrument. The Helium cell gas mode of the Agilent 7700× was used to measure Ti, V, Co, Ni, Cu, Zn, As, Mo and W while removing polyatomic interferences. The external precision and accuracy of the analyses were assessed by measuring as unknown four rock standards: BEN and BIR basalts, JP-1 peridotite and UBN serpentinite. Our results show good agreement between

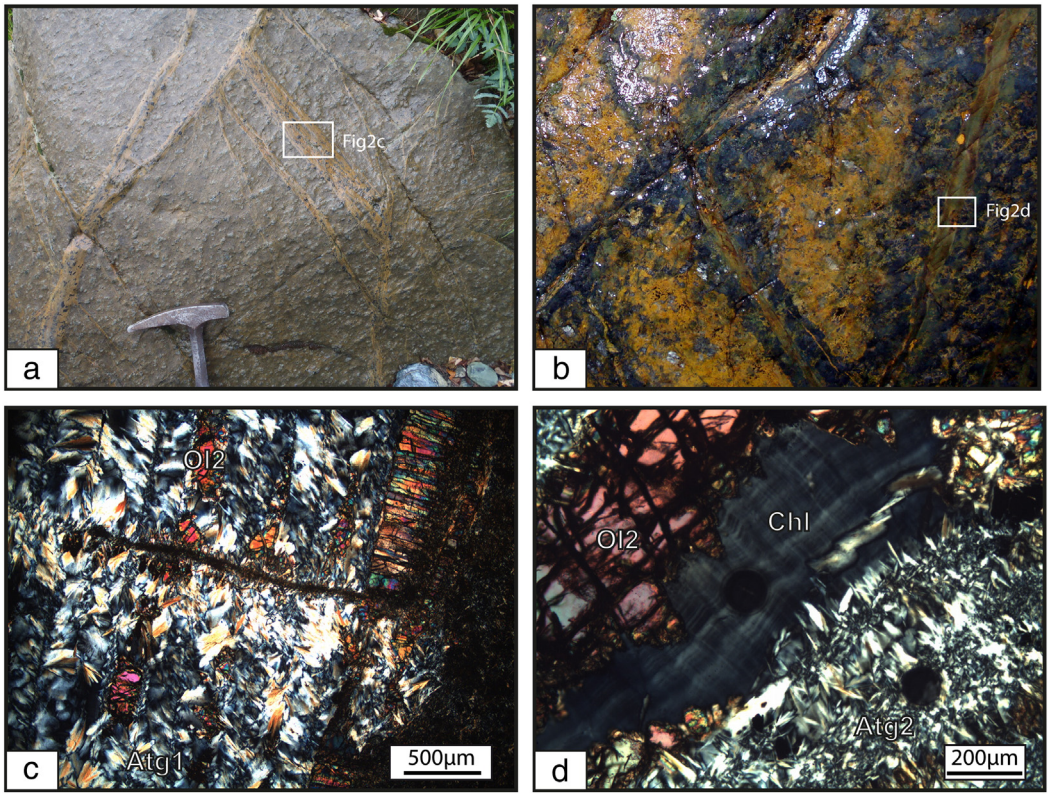

Fig. 3. (a) Network of parallel metamorphic veins crossing the SSP. The vein is orange with a white centre in relief at the outcrop surface. (b) MS crossed by relief metamorphic veins. The veins are zoned: their centre is orange (Ol2) and green (chlorite or Atg1) and the rims are dark blue (Atg2). The contact with the host rock is diffused. (c) Microphotograph (cross polarized light) of the centre part of a metamorphic vein crossing the SSP. Secondary olivine (Ol2) grows into parallel fractures cutting prograde antigorite. (d) Microphotograph (plane polarized light) of a relief vein crossing MS. Vein centre is composed of secondary olivine and chlorite (Chl). Retrograde antigorite replaces these two minerals. (For interpretation of the references to color in this figure legend, the reader is referred to the web version of this article.)

Table 1
Sample major and modal composition.

Rock	LZ35b	LZ19	LZ17a	LZ7	LZ27a1	LZ34d	LZ30	LZ26c	LZ26a	RO1	LZ8b	LZ14b	LZ5
Nature	Lherz	Lherz	Lherz	Dunite	MS	MS	MS	MS	FS	FS	FS	FS	FS
Protholite					Lherz	Lherz	Harz	Harz					
SiO_2	43.21	41.89	42.64	40.20	40.03	40.08	39.70	40.51	40.44	39.70	38.82	39.03	37.86
Al_2O_3	4.17	2.99	2.64	0.52	2.33	3.27	2.30	2.55	2.35	2.85	2.24	2.37	1.79
Fe_2O_3	8.19	8.87	8.86	6.82	8.45	7.30	6.16	5.78	5.58	8.14	9.73	8.42	8.09
MgO	36.42	38.58	39.49	43.38	38.55	36.47	39.77	38.52	39.01	36.04	37.06	38.13	35.94
CaO	3.95	3.13	2.62	0.10	1.46	3.31	–	1.09	0.05	2.10	0.09	0.02	1.57
Na_2O	0.44	0.15	0.09	–	0.34	0.31	0.10	–	–	0.22	0.11	0.35	0.07
K_2O	–	–	–	–	0.25	0.21	0.08	–	–	0.17	0.89	0.32	–
TiO_2	0.16	0.12	0.09	0.01	0.07	0.12	0.03	0.02	0.03	0.10	0.09	0.07	0.09
MnO	0.13	0.13	0.13	0.09	0.14	0.08	0.12	0.10	0.12	0.12	0.10	0.04	0.12
H_2O^+	0.06	–	0.13	0.07	0.10	0.00	0.02	0.08	0.10	0.06	0.08	−0.01	0.07
H_2O^-	2.43	3.43	2.96	8.46	7.83	8.88	11.72	10.92	11.75	10.40	11.02	11.35	14.24
Total	99.15	99.29	99.64	99.64	99.53	100.02	100.00	99.57	99.43	99.90	100.22	100.10	99.84
MODE													
Serp	0.08	0.16	0.14	0.16	0.75	0.74	0.97	0.91	0.96	0.77	0.79	0.94	0.73
Ol	0.64	0.63	0.67	0.71	0.07	0.03	–	0.03	0.03	0.13	<0,01	–	0.09
CPx	0.08	0.08	0.06	–	0.04	0.04	–	0.04	–	0.07	<0,01	–	0.03
Opx	0.09	0.06	0.07	0.1	–	–	–	–	–	–	–	–	–
Chl	–	–	–	0.03	0.12	0.09	<0,01	0.02	–	0.02	0.06	0.02	0.11
Tre	–	–	–	–	0.02	0.1	–	–	–	<0,01	0.13	–	0.04
Pl	0.11	0.07	0.06	–	–	–	–	–	–		–	–	–
Other	<0,01	<0,01	<0,01	<0,01	<0,01	<0,01	0.02	<0,01	<0,01	<0,01	<0,01	0.04	<0,01

The modal composition was obtained by calculation. $H2O^+$: loss by evaporation; $H2O^-$: loss on ignition; MS: Massive Serpentinite; FS: Foliated Serpentinite.

Table 2
Whole rock trace element analysis of the different lithologies composing the massif.

Sample	LZ35b	LZ19	LZ17a	LZ7	LZ27A	LZ34d	LZ30	LZ26c	LZ26a	RO1	LZ8b	LZ14b	LZ5
Nature	Lherz	Lherz	Lherz	Dunite	MS	MS	MS	MS	FS	FS	FS	FS	FS
Li	3.097	0.803	2.828	0.606	1.144	0.446	0.006	0.081	0.027	0.161	0.049	0.005	2.003
Sc	13.372	11.751	13.041	5.091	7.873	10.646	11.582	12.483	11.233	12.684	9.182	11.431	8.903
Ti*	0.085	0.064	0.049	0.002	0.041	0.069	0.023	0.012	0.015	0.056	0.054	0.040	0.052
V	72.078	61.763	65.530	18.784	37.480	57.292	54.404	61.188	50.867	65.646	58.611	56.825	47.017
Co	8.319	9.100	9.924	8.124	9.728	8.577	7.141	6.923	7.613	9.786	9.393	7.981	9.577
Ni*	0.199	0.224	0.211	0.259	0.213	0.211	0.089	0.120	0.115	0.225	0.128	0.182	0.224
Cu	31.382	18.096	21.414	0.499	4.116	6.342	2.785	6.179	7.492	9.372	11.577	1.574	11.290
Zn	43.493	47.981	42.820	38.711	35.278	36.180	43.304	38.103	37.225	50.157	47.145	28.871	38.504
As	0.057	0.049	0.046	0.037	0.043	0.053	1.231	0.034	0.043	0.127	0.041	0.089	0.057
Rb	0.084	0.059	0.032	0.044	0.055	0.077	0.012	0.005	0.017	0.104	0.029	0.051	0.056
Sr	19.158	5.436	1.282	0.999	7.411	9.986	0.062	0.227	0.152	1.821	0.537	0.286	6.083
Y	3.999	3.398	2.130	0.131	1.711	3.008	0.463	1.126	1.203	2.455	1.522	0.593	1.896
Zr	7.797	4.800	1.304	0.210	2.621	4.470	0.354	0.759	0.980	2.629	2.006	0.875	3.456
Nb	0.035	0.005	0.004	0.014	0.016	0.027	0.003	0.003	0.006	0.027	0.016	0.017	0.003
Mo	0.013	0.020	0.022	0.031	0.005	0.017	0.016	0.043	0.024	0.068	0.025	0.047	0.030
Cd	0.033	0.027	0.025	0.005	0.014	0.028	0.009	0.012	0.006	0.024	0.006	0.015	0.018
Sb	0.004	0.005	0.006	0.004	0.004	0.008	0.110	0.007	0.004	0.012	0.008	0.015	0.010
Cs	0.022	0.002	0.013	0.013	0.009	0.024	0.001	0.000	0.001	0.062	0.009	0.006	0.018
Ba	0.985	0.168	0.242	0.275	0.204	0.364	0.338	b.d.l.	b.d.l.	8.886	0.804	0.185	0.724
La	0.169	0.097	0.007	0.016	0.086	0.127	0.004	0.005	0.028	0.050	0.025	0.053	0.055
Ce	0.674	0.441	0.047	0.040	0.340	0.500	0.006	0.019	0.089	0.201	0.098	0.110	0.255
Pr	0.135	0.090	0.020	0.006	0.064	0.099	0.002	0.005	0.016	0.053	0.021	0.028	0.056
Nd	0.855	0.601	0.200	0.037	0.392	0.641	0.013	0.044	0.109	0.390	0.151	0.165	0.369
Sm	0.345	0.251	0.123	0.012	0.153	0.256	0.008	0.025	0.052	0.186	0.079	0.063	0.157
Eu	0.154	0.110	0.057	0.007	0.075	0.105	0.007	0.009	0.002	0.091	0.020	0.009	0.062
Gd	0.594	0.458	0.255	0.016	0.249	0.437	0.024	0.059	0.123	0.353	0.175	0.104	0.292
Tb	0.104	0.083	0.050	0.003	0.044	0.077	0.005	0.012	0.024	0.064	0.036	0.019	0.051
Dy	0.761	0.616	0.388	0.021	0.325	0.566	0.050	0.113	0.194	0.484	0.296	0.136	0.379
Ho	0.164	0.135	0.088	0.005	0.071	0.121	0.015	0.032	0.046	0.105	0.068	0.029	0.082
Er	0.458	0.385	0.256	0.015	0.207	0.340	0.060	0.124	0.136	0.303	0.212	0.081	0.228
Tm	0.067	0.057	0.039	0.003	0.031	0.051	0.013	0.024	0.022	0.044	0.034	0.013	0.035
Yb	0.432	0.372	0.263	0.023	0.208	0.330	0.111	0.182	0.150	0.286	0.225	0.088	0.221
Lu	0.072	0.062	0.046	0.006	0.036	0.057	0.022	0.035	0.026	0.049	0.039	0.015	0.039
Hf	0.232	0.156	0.067	0.006	0.083	0.145	0.030	0.046	0.043	0.108	0.074	0.040	0.108
Ta	0.0037	0.0013	0.0004	0.0007	0.0013	0.0028	0.0002	0.0002	0.0004	0.0019	0.0012	0.0003	0.0007
W	0.025	0.017	0.004	0.013	0.006	0.051	0.010	0.005	0.004	0.009	0.035	0.006	0.010
Pb	b.d.l.	0.060	b.d.l.	b.d.l.	b.d.l.	b.d.l.	0.112	b.d.l.	b.d.l.	0.139	b.d.l.	0.141	b.d.l.
Th	0.005	0.001	0.001	0.001	0.002	0.003	0.001	b.d.l.	0.001	0.004	0.002	0.002	0.001
U	0.0018	0.0004	0.0004	0.0007	0.0009	0.0010	0.0004	0.0003	0.0008	0.0011	0.0007	0.0060	0.0014

In ppm or *in %; b.d.l.: below detection limit.

measured values and expected values for the international standards, and external reproducibility is within 0–5% for Sc, Ti, V, Ni, Cu, As, Rb, Sr, Y, Zr, Nb, Mo, Cd, Sb, Cs, Ba, La, Ce, Nd, Sm, Eu, Gd, Tb, Ho, Tm, Lu, Pb, Th and U, it is within 5–10% for Li, Co, Pr, Dy, Er, Yb, Hf, Ta and W. The limits of detection, the procedural blank contributions and the values obtained for rock standards BEN, BIR, JP-1 and UBN during this study are reported in Appendix A.

3.2. In situ analyses

Mineral major and trace element analyses were performed on: (1) 2 samples of SSP (LZC02, LZ24 Fig. 2a–b) in which primary mineral as well as lizardite and antigorite veins have been analyzed. (2) 2 samples of MS (LZ26c and LZ27a1, Fig. 2c), and 2 samples of metamorphic veins crossing the MS (LZ34b–c, Fig. 3b, d). In those samples, the relative chronology between the different phases (prograde antigorite, dehydrated olivine and retrograde antigorite) is well established. (3) 1 sample of FS (RO3, Fig. 2d) that is principally composed of retrograde antigorite.

Electron microprobe analyses of major elements are reported in Debret et al. (2013). In situ LA-ICPMS measurement of trace elements were conducted on 100 μm thick polished section realized on the same rock piece as the one used by Debret et al. (2013) for electron microprobe analyses. In situ trace element compositions were determined at Montpellier 2 University on a ThermoFinnigan Element 2 High Resolution-Inductively Coupled Plasma-Mass Spectrometer (HR-ICP-MS) using a single collector double-focusing sector field Element XR (eXtended Range) coupled with laser ablation (LA) system, a Geolas (Microlas) automated platform housing a 193 nm Compex 102 laser from LambdaPhysik.

Oxide level, measured using the ThO/Th ratio, was below 0.7%. ^{29}Si was used as internal standard. For each serpentine texture, ^{29}Si was calibrated from the mean value of several microprobe analyses. Concentrations were calibrated against the NIST 612 rhyolitic glass using the values given in Pearce et al. (1997). Data were subsequently reduced using the GLITTER software (Van Achterberg et al., 2001) using the linear fit to ratio method. This typically resulted in a 5 to 10% precision (1sigma) for most analyses, evaluated by repeated analyses of reference basalt BIR (Appendix B). Detection limits were between <1 and 50 ppb for most trace elements, between 0.06 and 1, 3 and 4 ppm for Li, B, As, Zn, Cr and Ti, and between 1 and 10, 30 and 50 ppm for Ni, Ca and Si for respective spot size of 102, 77 and 51 μm.

The different varieties of serpentine were primarily identified in thin sections, and then characterized by Raman spectroscopy (Laboratoire de Géologie de Lyon, France: Debret et al., 2013). Due to the large beam size (up to 102 μm) and the small grain size of serpentine, it was impossible to analyse serpentine varieties without dusty inclusions of magnetite or other minor secondary phases. Nevertheless, LA-ICPMS analyses yield a good reproducibility suggesting that the analyses are representative of serpentine textural and chemical evolution during prograde metamorphism.

4. Results

4.1. Whole rock major and trace element compositions

Results of whole rock analyses are reported in Tables 1 and 2 and illustrated in Figs. 4 and 5. Analyses of SSP are in good agreement with previous studies (Fig. 4; Bodinier, 1988; Piccardo et al., 2007a, 2007b; Kaczmarek and Müntener, 2010): they have comparable SiO_2 (40.20–43.21 wt.%), MgO (36.42–43.38 wt.%) and Al_2O_3 (0.52–4.17 wt.%). Al_2O_3 varies according to rock type (Bodinier, 1988): the highest Al_2O_3 concentrations correspond to the plagioclase lherzolites (Al_2O_3 = 2–4 wt.%) and the lowest Al_2O_3 to the dunite (Al_2O_3 <1 wt.%).

Lherzolite compositions (LZ17-19-35, Fig. 5) are similar to previously analyzed impregnated lherzolites (Piccardo et al., 2007a; Kaczmarek and Müntener, 2010). Their patterns are characterized by a depletion in LREE (Ce_N/Yb_N = 0.05–0.43; N: C1-chondrites normalized; Fig. 5a) and a flat medium and heavy rare earth element (M-HREE) segment (Gd_N/Yb_N = 0.80–1.14 and Eu/Eu^* = 0.95–1.03). Slightly concentration variations are observable at massif scale (Yb = 1.5–2.5 × C1-chondrites). They are attributed to the modal composition of the lherzolite: the Cpx poor lherzolites have a lower concentration and higher LREE depletion than Cpx rich lherzolites. The extended trace element patterns of lherzolites present a U-shaped pattern (Fig. 5b) with a weak enrichment in U and a depletion in Y and Sr (Sr_n/Nd_n = 0.38–1.47; n = normalized to primitive mantle values) relative to their

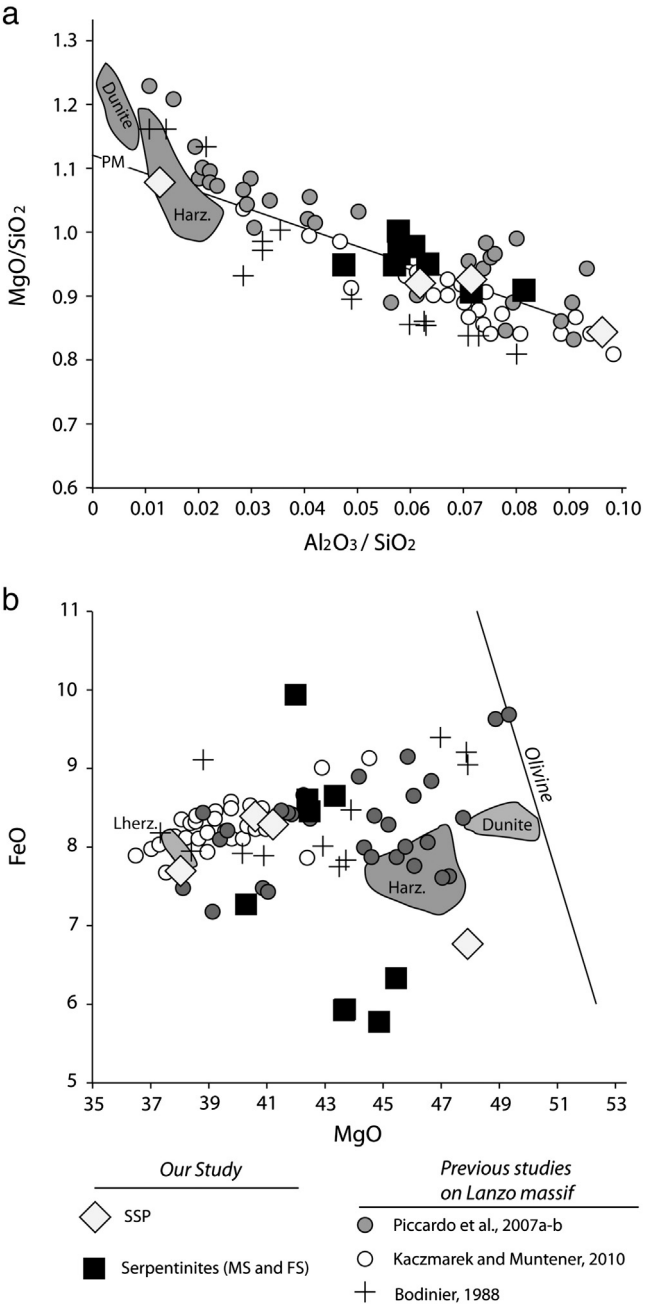

Fig. 4. Bulk rock major element composition of the SSP and serpentinites (MS and FS) illustrated in (a) Al_2O_3 versus MgO/SiO_2 and (b) MgO (wt.%) versus FeO (wt.%). On Fig. 4a, the dark line represents the silicate Earth differentiation trend and the primitive mantle ratio (PM, Kaczmarek and Müntener, 2010). On Fig. 4b, the dark line represents the stoichiometric variations of olivine Fe–Mg composition. Published data from Lanzo massif are shown for comparison: Bodinier (1988), Piccardo et al. (2007a, 2007b) and Kaczmarek and Müntener (2010). Abyssal peridotites poles (Lherzolite, Harzburgite and Dunites) are shown in shaded area and are from Godard et al. (2008).

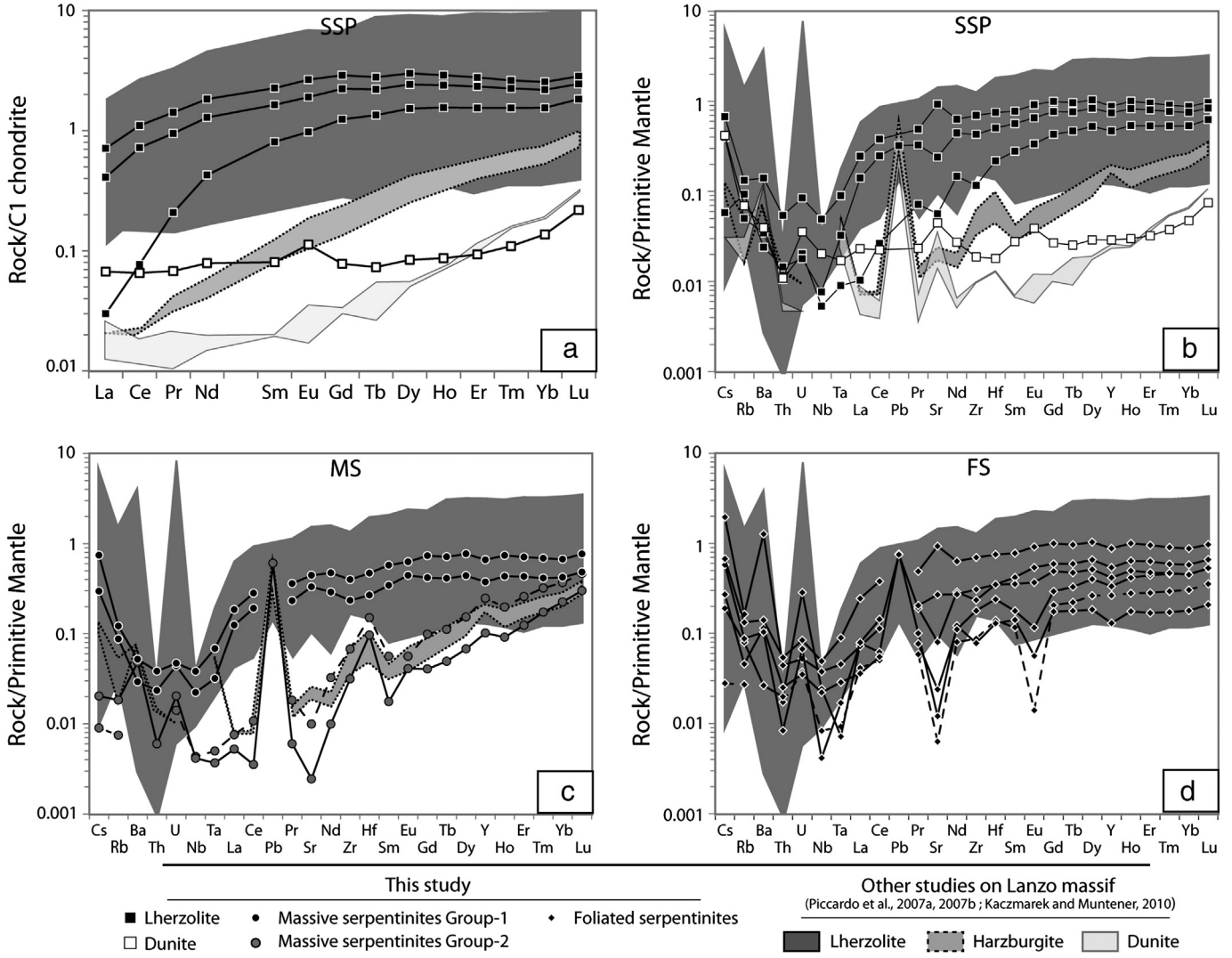

Fig. 5. Whole rock patterns of the different lithologies composing the Lanzo massif. (a) and (b–c–d) patterns are respectively chondrite and primitive mantle normalized; normalizing values are from Sun and McDonough (1989). Symbols are indicated in the figure. Previous analyses of Lanzo peridotites are shown in comparison (shaded areas). (a) Whole rock REE patterns of different type of SSP. (b) Spidergram of SSP. (c) Spidergram of MS. MS analyses do not differ from SSP analysis. Dashed line: LZ26c (massive serpentinite lens embedded by foliated serpentinite). (d) Spidergram of FS. Dashed line: LZ26a (foliated serpentinite embedding LZ26c).

neighboring elements. Dunitic sample (LZ7) has a concave upward pattern (Yb = 0.14 × C1-chondrites) characterized by an enrichment in HREE relative to MREE (Gd_N/Yb_N = 0.57) and by a positive Eu anomaly (Eu/Eu^* = 1.42). Compared to available dunite data (Gd_N/Yb_N = 0.16–0.18), this sample is enriched in L-MREE (Fig. 5a). No harzburgite was analyzed during this study but Bodinier (1988) and Piccardo et al. (2007a, 2007b) report their presence in the studied area. Their REE pattern (Fig. 5a) is characterized by positive slope from LREE to HREE with a low LREE/HREE ratio (Ce_N/Yb_N = 0.03–0.04). Its extended trace element pattern presents a U-shaped pattern with an alkali enrichment relative to LREE (Ba_n/Ce_n = 9.07). It displays U, Ta, Pb, Sr, Zr, Hf and Y positive anomalies relative to their neighboring elements (Fig. 5b).

FME concentrations of SSP are listed in Table 2. They range from 0.06 to 0.31 ppm for Li, from0.004 to 0.006 ppm for As and 0.004 to 0.007 ppm for Sb.

Compared to peridotites, the serpentinites (MS and FS) display a lower SiO_2 (=37.87–40.51 wt.%) content and similar MgO (=35.94–39.77 wt.%) and Al_2O_3 (=1.79–3.27 wt.%) contents.

Within the MS, two groups are distinguished according to their trace element composition (Fig. 5c). The Group-1 (Samples LZ34 and LZ27) has REE, trace element patterns and concentration identical to Lanzo massif lherzolites. It is characterized by a LREE depletion (Ce_N/Yb_N = 0.42–0.45), a flat M-HREE (Gd_N/Yb_N = 0.99–1.10) and display a depletion in alkali relative to LREE (Rb_n/La_n = 0.66–0.70). The Li contents range from 0.05 to 0.11 ppm, the As contents from 0.005 to 0.004 ppm and the Sb contents from 0.006 to 0.007 ppm. Group-2 samples (LZ26c and LZ30) have patterns and concentration similar to Lanzo massif harzburgite. It displays a similar LREE/HREE ratio (Ce_N/Yb_N = 0.02–0.03) but its trace element pattern differs from harzburgite pattern by a negative anomaly in Sr (Sr_n/Nd_n = 0.25–0.30). Those serpentinites have <0.001–0.008 ppm Li, 0.003–0.123 ppm As and 0.014–0.019 ppm Sb.

FS have homogenous patterns, similar to lherzolites (Fig. 5d). They are characterized by a LREE depletion (Ce_N/Yb_N = 0.12–0.35) and a relatively flat M-HREE Gd_N/Yb_N = 0.64–1.09. Nevertheless, compared to lherzolites, they show a variable negative Eu anomaly (Eu/Eu^* = 0.09–1.07). Trace element patterns of FS are similar to the U-shaped pattern of lherzolite except that they show variable negative Sr (Sr_n/Nd_n = 0.08–0.99). The Li content of foliated serpentinites varies from <0.001 to 0.20 ppm, the As from 0.004 to 0.13 and the Sb from 0.005 to 0.10 ppm.

4.2. In situ analyses

Analyses were conducted using an in-house modified ablation cell of ca. 30 cm^3, which resulted in a shorter washout time and an improved sensitivity compared with the initial larger ablation cell. Ablation experiments were conducted in a helium atmosphere, which enhances sensitivity and reduces inter-element fractionation (Gunther and Heinrich, 1999). The helium gas and particles from the sample were then mixed with argon before entering the plasma. Signals were acquired in Time Resolved Acquisition, devoting 2 min 30 s for the blank and 1 min for measurement of the analyses. The laser was fired using an energy density of 12 J cm^{-2} at a frequency of 6 Hz (samples LZ34b.c, 24, LZC02 and RO3), 7 Hz (sp. LZ27a1, LZ34b and RO3) and 8 Hz (sp. LZ26c and LZ34b) and using a spot size of 102 μm (sp. LZ26c, 27a1, 34b.c and RO3), 77 μm (sp. LZ34b, 24 and LZC02) and 51 μm (sp. LZC02) depending on the size of analyzed phases. Before measurement, the laser was pre-ablated using a larger spot size to clean the thick section surface. The acquisition spot size was larger than serpentine grains, but it was necessary to get good accuracy on our results. This resulted in an average sensitivity of ~1000, 400, 200 cps/ppm for B, Ti, Cr, Zn and As, 2000, 900, 500 cps/ppm for Li and Ba and 3000, 1000, 800 cps/ppm for other trace elements for the 102, 77 and 51 μm spot sizes respectively.

4.2.1. Mantle minerals

In order to establish the initial composition of the mantle peridotites, in situ trace analyses were performed on olivine, orthopyroxene and clinopyroxene. Measured concentrations are shown in Table 3 and in Fig. 6.

The clinopyroxene composition (Yb = 12–17 × C1-chondrite) is relatively homogenous at the massif scale. It has a LREE depletion (Ce_N/Yb_N = 0.07–0.48), a flat pattern in the MREE region, a weak HREE depletion (Gd_N/Yb_N = 1.08–1.45) and a negative Eu anomaly (Eu/Eu^* = 0.67–0.81). Among clinopyroxene patterns, we distinguish two groups characterized by different LREE-depletions ($Ce_N/Yb_N \approx 0.07$ and 0.45). This LREE-variation has already been observed in Lanzo peridotites: it results from melt/peridotite interaction during massif exhumation in an OCT context (see Piccardo et al., 2007a, 2007b). Clinopyroxene extended patterns possess weak negative Y and Zr anomaly relative to elements of similar compatibility and significant negative Sr (Sr_n/Nd_n = 0.01–0.08) and Pb (Pb_n/Ce_n = 0.06–0.23) anomalies.

Orthopyroxene compositions (Yb = 3–4 × C1-chondrite) are intermediate between clinopyroxene and olivine. They display a low LREE/HREE ratio (Ce_N/Yb_N = 0.004–0.013, Gd_N/Yb_N = 0.12–0.20). Extended trace element patterns are characterized by positive slope from LREE to HREE with a positive Zr, Hf and Pb (Pb_n/Ce_n = 5–28) anomaly and a variable Sr anomaly (Sr_n/Nd_n = 0.05–3.69) relative to elements of similar compatibility. Orthopyroxene patterns are similar to those reported in the literature for peridotites of Lanzo massif (Piccardo et al., 2007a, 2007b; Kaczmarek and Müntener, 2010).

Compared to other primary minerals, olivines are depleted in REE (Yb = 0.01–0.4 × C1-chondrite). They display a concave pattern with high HREE content relative to LREE ($Ce_N/Yb_N \approx 0.020$) and MREE (Gd << 1 ppb) content. They have positive Sr ($Sr_n/Nd_n \approx 14$) and a Pb (Pb_n/Ce_n = 57–112) anomaly relative to elements of similar compatibility.

The FME content of primary minerals (Table 3) is similar to those reported in oceanic and ophiolites environments (Fig. 7).

4.2.2. Serpentine in slightly serpentinized peridotites

The REE and trace element compositions of lizardite veins crossing the orthopyroxene (Liz–Opx, Yb = 2–3 × C1-chondrite) are similar to orthopyroxene composition (Fig. 6a–b, Table 3). REE patterns display a positive slope from LREE to HREE (Ce_N/Yb_N = 0.006–0.038) with a positive Eu anomaly (Eu/Eu^* = 1.74–3.60). Extended trace element patterns display a U-shaped pattern with positive Sr (Sr_n/Nd_n = 0.69–12.35), Pb (Pb_n/Ce_n = 1.91–11.23) and Ta (Ta_n/Ce_n = 1.11–1.28) anomalies, and an alkali enrichment relative to LREE (Ba_n/Ce_n = 3.83–7.22).

Lizardite veins crossing the olivine (Liz–Ol) have REE and trace element contents near the detection limit (Yb = 0.1–0.2 × C1-chondrite, Fig. 6a-b, Table 3). Their REE patterns display a LREE and MREE depletion relative to HREE (Ce_n/Yb_n = 0.01–0.02) with a positive Eu anomaly relative to element of similar compatibility. Extended patterns present a concave pattern with an alkali enrichment (Ba_n/Ce_n = 8.38–16.33) and positive Ta ($Ta_n/Ce_n \approx 34$), Pb (Pb_n/Ce_n = 85–269) and Sr ($Sr_n/Nd_n \approx 5.9$) anomalies.

Mesh and bastite texture have similar REE and trace contents (Fig. 6a–b, Table 3). They display a low LREE/HREE ratio (Ce_N/Yb_N <0.01) and have an intermediate composition (Yb = 0.3–0.4 × C1-chondrite) between orthopyroxene and olivine (Fig. 6a). They have a positive Eu anomaly ($Eu/Eu^* \approx 7.54$). Extended patterns display a positive Pb (Pb_n/Ce_n = 15–174) anomaly and variable Sr (Sr_n/Nd_n = 0.33–1.02) and Ba (Ba_n/Ce_n = 0.88–8.04) anomalies (Table 3, Fig. 5b).

Lizardites have a high B (1.8–75.1 ppm) and similar Li (0.24–2.55 ppm), As (0.10–0.15 ppm), Sb (<0.01), Ba (0.03–1.16 ppm) and Rb (0.064 ppm) relative to mantle minerals (Table 3, Fig. 6).

Antigorite veins crossing the clinopyroxene (Atg–Cpx, Yb = 4–7 × C1-chondrite) have an intermediate composition between Cpx and Opx (Fig. 6c and Table 3). Their REE patterns display a LREE depletion relative to MREE (Ce_N/Yb_N = 0.03–0.04) and a flat MREE–HREE (Gd_N/Yb_N = 0.90–1.18). They show a negative Eu anomaly (Eu/Eu^* = 0.09–0.25). Extended trace element patterns display negative Sr (Sr_n/Nd_n = 0.03–0.04) and Pb ($Pb_n/Ce_n \approx 0.33$) anomalies.

REE patterns of antigorite veins crossing the orthopyroxene (Atg–Opx, Yb = 0.9–1.1 × C1-chondrite) show a LREE depletion relative to M–HREE (Ce_N/Yb_N = 0.02–0.05) and a weak positive slope from MREE to HREE (Gd_N/Yb_N = 0.43–0.64). They display a negative Eu anomaly (Eu/Eu^* = 0.64–0.81). Extended trace element patterns (Fig. 6c) show a positive Sr (Sr_n/Nd_n = 0.53–0.63), Ba (Ba_n/Ce_n = 0.47–2.20), U and Pb ($Pb_n/Ce_n \approx 26$) relative to element of similar behavior.

Antigorite veins crossing the olivine (Atg–Ol, Yb < 0.3 × C1-chondrite) show a similar pattern (6c) as Atg–Opx and Atg–Cpx: a LREE depletion relative to MREE (Ce_N/Yb_N = 0.02–0.05) and a flat H–MREE (Tb_N/Yb_N = 0.41–1.17). They do not display Eu anomalies.

Antigorite veins have similar Li (0.82–1 ppm), As (0.08–0.27) and Sb (<0.01) and low B (0.87–28.89 ppm), Ba (0.07–0.11) and Rb (<0.044 ppm) contents compared to mantle minerals and lizardites analyzed during this study (Fig. 7 and Table 3).

4.2.3. Antigorite of massive and foliated serpentinites

Among prograde antigorites, two groups are distinguished on the basis of their trace element concentrations (Fig. 6d–e).

(1) The first group corresponds to prograde antigorite in the lherzolite serpentinites (Fig. 6d). Its composition (Yb = 0.4–5 × C1-chondrite) is intermediate between all primary phases of the peridotite (clinopyroxene, orthopyroxene and olivine). REE patterns have a LREE depletion relative to M–HREE (Ce_N/Yb_N = 0.30–0.38), a flat M–HREE (Gd_N/Yb_N = 0.85–0.97) and a variable Eu anomaly (Eu/Eu^* = 0.90–1.18). Extended patterns present a U-shaped pattern with an alkali enrichment (Ba_n/Ce_n = 0.15–0.27) and a variable Sr (Sr_n/Nd_n = 0.25–1.23) and positive U (U_n/Nb_n = 1.45–2.75) and Hf anomalies.
(2) The second group of prograde antigorite has been observed in harzburgite serpentinites (Fig. 6e). Their patterns are characterized by an intermediate composition (Yb = 0.7–1.1 × C1-chondrite) between orthopyroxene and olivine. It displays a low LREE/HREE ratio (Ce_N/Yb_N = 0.02–0.04) with a flat HREE and a negative Eu anomaly (Eu < 1 ppb). Extended to trace element patterns present an alkali depletion (Ba_n/Ce_n = 0.25–0.35) with positive Pb (Pb_n/Ce_n = 5.35–8.22), U (U_n/Nb_n =

Table 3
Trace element analyses (LA-ICPMS) for minerals composing the SSP, MS and FS.

Rock	Lherzolite														
Sample	LZ24	LZC02	LZC02	LZC02	LZC02	LZ34b	LZC02	LZC02	LZC02	LZC02	LZC02	LZC02	LZC02	LZC02	LZ24
Spot size	77	77	77	77	77	102	77	77	77	77	77	77	77	77	77
Mineral	Ol	Ol	Opx	Opx	CPx	CPx	Liz–Ol	Liz–Ol	Liz–Ol	Liz–Opx	Liz–Opx	Mesh	Bastite	Atg1–Ol	Atg1–Ol
Li	4.910	1.410	0.660	0.302	0.470	0.263	b.d.l.	b.d.l.	0.243	0.622	0.880	b.d.l.	b.d.l.	n.d.	b.d.l.
B	0.995	0.489	0.697	1.210	0.679	0.754	17.250	50.630	21.170	65.700	68.330	21.330	22.960	3.220	0.872
Si*	19.165	19.165	26.177	26.177	24.774	24.307	17.763	17.763	17.763	18.230	20.567	20.100	20.100	20.100	20.100
Ca*	0.029	0.028	1.310	0.789	15.735	15.403	0.015	0.018	0.014	0.207	0.130	0.024	0.024	b.d.l.	0.069
Sc	7.060	3.280	36.750	34.190	76.060	72.090	2.341	3.140	2.880	27.870	26.400	3.610	3.240	4.950	3.830
Ti	63.070	33.870	1517.940	1369.030	3582.190	5048.420	81.680	33.990	27.620	1163.930	1197.020	39.780	39.880	58.310	20.650
V	1.109	1.431	188.690	168.050	362.160	326.280	0.826	1.741	1.673	127.310	136.130	4.350	2.755	22.860	21.760
Cr*	0.001	0.002	0.537	0.402	0.983	0.866	0.001	0.002	0.002	0.358	0.342	0.008	0.002	0.003	0.003
Co	191.340	148.000	58.030	56.360	25.530	23.830	37.470	63.170	33.880	17.800	19.610	42.980	50.260	52.440	59.800
Ni*	0.390	0.337	0.079	0.070	0.043	0.037	0.129	0.221	0.197	0.051	0.050	0.239	0.239	0.133	0.152
Cu	0.189	b.d.l.	b.d.l.	b.d.l.	0.356	b.d.l.	3.010	1.728	4.280	1.240	1.216	6.310	6.170	0.520	0.817
Zn	47.120	52.230	40.000	41.440	12.330	10.270	11.510	13.350	12.470	37.360	38.910	14.490	9.740	11.110	20.600
As	n.d.	b.d.l.	b.d.l.	b.d.l.	0.173	0.304	0.096	0.128	b.d.l.	0.127	0.164	n.d.	b.d.l.	b.d.l.	b.d.l.
Rb	b.d.l.	b.d.l.	b.d.l.	b.d.l.	b.d.l.	0.017	b.d.l.	b.d.l.	b.d.l.	b.d.l.	b.d.l.	b.d.l.	b.d.l.	b.d.l.	b.d.l.
Sr	0.478	b.d.l.	0.595	0.322	0.523	7.320	0.258	0.269	0.263	1.092	1.127	0.278	0.289	0.324	0.679
Y	0.113	0.033	3.550	2.558	27.140	29.800	0.156	0.032	0.012	2.871	1.853	0.356	0.343	0.319	0.287
Zr	0.048	0.010	1.850	1.062	14.620	50.360	0.032	n.d.	0.018	1.026	0.733	0.161	0.072	0.181	0.103
Nb	b.d.l.	b.d.l.	0.005	n.d.	b.d.l.	0.068	n.d.	b.d.l.	b.d.l.	b.d.l.	b.d.l.	0.002	b.d.l.	n.d.	b.d.l.
Sb	b.d.l.	b.d.l.	b.d.l.	b.d.l.	0.009	b.d.l.	n.d.	b.d.l.	b.d.l.	b.d.l.	b.d.l.	n.d.	0.006	b.d.l.	b.d.l.
Cs	b.d.l.	b.d.l.	b.d.l.	b.d.l.	b.d.l.	b.d.l.	b.d.l.	b.d.l.	b.d.l.	b.d.l.	b.d.l.	b.d.l.	b.d.l.	b.d.l.	b.d.l.
Ba	0.077	b.d.l.	0.136	0.217	b.d.l.	b.d.l.	0.081	0.059	0.033	0.365	0.290	n.d.	0.081	b.d.l.	n.d.
La	0.0003	b.d.l.	0.0005	b.d.l.	0.0273	0.7650	b.d.l.	0.0003	b.d.l.	0.0018	0.0013	b.d.l.	b.d.l.	b.d.l.	0.0020
Ce	0.0022	0.0009	0.0100	0.0081	0.6690	4.7600	0.0013	0.0016	0.0010	0.0242	0.0102	0.0173	0.0026	0.0049	n.d.
Pr	b.d.l.	b.d.l.	0.0075	0.0039	0.3250	1.1290	b.d.l.	b.d.l.	0.0003	0.0093	0.0027	0.0082	0.0013	0.0019	0.0015
Nd	0.0022	b.d.l.	0.0873	n.d.	3.4300	7.7400	0.0028	b.d.l.	b.d.l.	0.1021	0.0154	0.0536	0.0181	0.0226	0.0069
Sm	b.d.l.	b.d.l.	0.0430	0.0259	2.1100	3.0900	b.d.l.	b.d.l.	b.d.l.	0.0410	b.d.l.	0.0041	b.d.l.	n.d.	b.d.l.
Eu	b.d.l.	b.d.l.	0.0206	n.d.	0.6340	0.9910	b.d.l.	b.d.l.	0.0055	0.0493	0.0348	0.0199	0.0160	0.0030	0.0051
Gd	b.d.l.	b.d.l.	0.1720	0.1000	3.8700	4.8600	b.d.l.	b.d.l.	b.d.l.	0.1460	0.0680	0.0132	0.0215	n.d.	n.d.
Tb	b.d.l.	b.d.l.	0.0419	0.0311	0.7050	0.8240	b.d.l.	b.d.l.	n.d.	0.0373	0.0294	0.0057	0.0046	0.0063	0.0019
Dy	0.0069	b.d.l.	0.5230	0.3170	5.0200	5.9400	0.0082	b.d.l.	b.d.l.	0.3990	0.2200	0.0428	0.0490	0.0583	0.0160
Ho	n.d.	0.0003	0.1406	0.0847	1.0490	1.1930	0.0025	0.0004	b.d.l.	0.1023	0.0729	0.0138	0.0091	0.0085	0.0043
Er	0.0111	b.d.l.	0.3740	0.3690	2.9400	3.3300	0.0071	0.0017	0.0018	0.3950	0.2920	0.0368	0.0362	0.0390	n.d.
Tm	0.0038	0.0003	0.0799	0.0698	0.4040	0.4540	0.0019	0.0018	0.0012	0.0741	0.0530	0.0066	0.0045	n.d.	n.d.
Yb	0.0626	0.0122	0.7170	0.5710	2.5200	2.7640	0.0351	n.d.	0.0161	0.5560	0.4390	0.0524	0.0710	0.0245	n.d.
Lu	0.0157	0.0038	0.1033	0.0982	0.3520	0.3520	0.0062	0.0041	0.0032	0.1014	0.0799	0.0140	0.0103	0.0047	0.0025
Hf	b.d.l.	b.d.l.	0.135	0.091	0.763	1.909	b.d.l.	b.d.l.	b.d.l.	0.067	0.050	0.003	0.004	b.d.l.	b.d.l.
Ta	b.d.l.	0.001	n.d.	b.d.l.	b.d.l.	0.011	0.001	b.d.l.	b.d.l.	0.001	b.d.l.	b.d.l.	b.d.l.	b.d.l.	b.d.l.
Pb	b.d.l.	0.005	n.d.	0.010	b.d.l.	0.032	0.011	0.016	0.028	0.005	0.012	0.027	0.046	0.014	0.009
Th	b.d.l.	b.d.l.	b.d.l.	b.d.l.	b.d.l.	0.0047	b.d.l.	b.d.l.	b.d.l.	b.d.l.	b.d.l.	b.d.l.	b.d.l.	b.d.l.	b.d.l.
U	b.d.l.	b.d.l.	b.d.l.	b.d.l.	b.d.l.	0.0028	b.d.l.	0.0001	b.d.l.	b.d.l.	b.d.l.	b.d.l.	b.d.l.	b.d.l.	b.d.l.

Rock	Lherzolite				Massive S.									Foliated S.	
Sample	LZC02	LZC02	LZC02	LZC02	LZ26c	LZ26c	LZ27	LZ27	LZ34b	LZ34b	LZ34b	LZ34c	LZ27	RO1	RO1
Spot size	51	77	51	77	102	102	102	102	102	102	102	102	102	102	102
Mineral	Atg1-Opx	Atg1-Opx	Atg1-CPx	Atg1-CPx	Atg1	Atg1	Atg1	Atg1	Atg2	Atg2	Atg2	Atg2	Atg2	Atg2	Atg2
Li	b.d.l.	n.d.	b.d.l.	0.710	b.d.l.	b.d.l.	n.d.	0.061	0.149	b.d.l.	b.d.l.	b.d.l.	b.d.l.	0.086	0.041
B	2.330	5.730	20.870	24.950	8.460	7.360	0.603	0.629	1.800	2.530	1.686	1.420	0.476	4.880	3.690
Si*	20.100	20.100	18.698	17.763	18.698	18.698	20.100	20.100	20.567	17.763	20.567	20.100	20.100	20.100	20.100
Ca*	0.369	0.008	0.032	0.057	0.019	0.014	0.003	0.002	0.003	0.004	0.005	0.006	0.005	0.005	0.006
Sc	15.030	12.110	15.460	32.630	18.740	17.240	6.450	7.480	11.110	11.180	11.910	8.400	7.390	11.080	8.880
Ti	1298.750	537.510	212.230	1843.460	193.230	146.680	29.360	26.830	34.140	32.540	63.270	34.150	29.210	41.000	35.860
V	120.980	126.980	25.450	162.350	113.520	93.010	34.930	25.440	17.780	21.410	19.530	31.160	41.740	48.100	30.990
Cr*	0.179	0.287	0.000	0.391	0.282	0.212	0.010	0.020	0.005	0.026	0.028	0.027	0.054	0.041	0.005
Co	47.260	50.280	5.560	39.410	16.060	19.740	68.640	66.860	70.180	58.650	69.570	70.210	69.170	77.300	78.070
Ni*	0.121	0.111	b.d.l.	0.016	0.003	0.003	0.162	0.154	0.164	0.140	0.163	0.140	0.163	0.077	0.070
Cu	b.d.l.	1.053	0.535	11.920	b.d.l.	b.d.l.	b.d.l.	n.d.	b.d.l.	0.049	n.d.	0.476	0.641	0.258	0.979
Zn	12.200	10.730	17.300	23.470	31.870	35.140	28.030	24.580	19.040	15.390	18.690	19.950	25.440	22.340	19.060
As	b.d.l.	b.d.l.	b.d.l.	0.237	n.d.	b.d.l.	b.d.l.	b.d.l.	0.087	n.d.	0.062	0.075	0.017	n.d.	0.023
Rb	b.d.l.	b.d.l.	b.d.l.	b.d.l.	b.d.l.	b.d.l.	0.067	0.070	b.d.l.	0.064	b.d.l.	0.019	0.016	0.030	0.046
Sr	0.875	0.612	0.301	0.435	0.080	0.040	0.662	0.484	0.271	0.374	0.491	0.537	1.118	0.356	0.316
Y	1.935	0.980	8.070	9.530	2.350	1.293	0.795	0.617	0.480	1.486	0.698	0.651	1.169	1.742	0.809
Zr	0.594	0.607	3.730	6.360	1.556	1.127	0.942	1.102	0.363	1.175	0.363	0.505	0.713	1.753	0.929
Nb	0.010	b.d.l.	b.d.l.	b.d.l.	0.001	0.001	0.004	0.003	b.d.l.	b.d.l.	0.002	b.d.l.	0.002	0.008	0.005
Sb	b.d.l.	0.005	b.d.l.	b.d.l.	b.d.l.	b.d.l.	b.d.l.	b.d.l.	n.d.	b.d.l.	b.d.l.	b.d.l.	n.d.	b.d.l.	0.001
Cs	b.d.l.	0.018	b.d.l.	b.d.l.	b.d.l.	b.d.l.	0.028	0.069	b.d.l.	0.042	b.d.l.	n.d.	0.008	n.d.	n.d.
Ba	0.067	0.111	0.078	0.157	0.018	n.d.	0.098	0.058	0.218	0.019	0.020	0.080	0.105	0.184	0.264
La	0.0024	b.d.l.	0.0029	0.0045	0.0103	n.d.	0.0243	0.0206	0.0102	0.0309	0.0164	0.0285	0.0472	0.0337	n.d.

(continued on next page)

Table 3 (*continued*)

Rock	Lherzolite				Massive S.									Foliated S.	
Sample	LZC02	LZC02	LZC02	LZC02	LZ26c	LZ26c	LZ27	LZ27	LZ34b	LZ34b	LZ34b	LZ34c	LZ27	RO1	RO1
Spot size	51	77	51	77	102	102	102	102	102	102	102	102	102	102	102
Ce	0.0362	0.0128	0.0918	0.1281	0.0183	0.0150	0.0926	0.0946	0.0528	0.1244	0.0613	0.0935	0.1816	0.1555	0.0810
Pr	0.0068	0.0051	0.0462	0.0663	0.0019	0.0023	0.0196	0.0188	0.0094	0.0267	0.0163	0.0202	0.0369	0.0343	0.0193
Nd	0.0880	0.0739	0.5590	0.7780	0.0174	0.0081	0.1144	0.1242	0.0627	0.1710	0.1019	n.d.	0.2390	0.2270	0.1313
Sm	0.0500	0.0211	0.4760	0.5650	0.0027	0.0048	0.0434	0.0354	0.0230	0.0850	0.0488	n.d.	0.0826	0.1125	0.0638
Eu	0.0191	0.0122	0.0178	0.0748	b.d.l.	b.d.l.	0.0201	0.0197	0.0050	0.0221	0.0091	0.0108	0.0362	0.0439	0.0245
Gd	0.1440	0.0790	0.8050	1.3910	0.0620	0.0216	0.1001	0.0710	0.0522	0.1480	0.0582	0.0800	0.1410	0.2120	0.1041
Tb	0.0303	0.0163	0.1740	0.2300	0.0154	0.0051	0.0160	0.0134	0.0097	0.0267	0.0140	0.0168	0.0261	0.0437	0.0211
Dy	0.3030	0.1310	1.4170	1.7950	0.1890	0.0892	0.1290	0.1041	0.0705	0.2110	0.1162	0.1070	0.1990	0.3540	0.1650
Ho	0.0547	0.0368	0.3150	0.3660	0.0618	0.0311	0.0301	0.0234	0.0177	0.0540	0.0270	0.0271	0.0417	0.0865	0.0376
Er	0.1940	0.1140	0.8870	1.1020	0.2170	0.1190	0.0865	0.0661	0.0558	0.1969	0.0815	n.d.	0.1279	0.2750	0.1298
Tm	0.0244	0.0181	0.1269	0.1431	n.d.	0.0195	0.0143	n.d.	0.0074	0.0267	0.0116	0.0145	0.0170	0.0400	0.0208
Yb	0.1860	0.1510	0.7420	0.9730	0.1570	0.0928	0.0853	0.0690	0.0662	0.2110	0.0881	0.1020	0.1351	0.2920	0.1640
Lu	0.0287	0.0285	0.1091	0.1255	0.0258	0.0171	0.0136	0.0146	0.0096	0.0320	0.0138	0.0124	0.0201	0.0491	0.0234
Hf	0.017	0.032	0.157	0.311	0.113	0.079	0.056	0.062	0.024	0.089	0.022	0.020	0.035	0.097	0.043
Ta	b.d.l.	n.d.	b.d.l.	b.d.l.	b.d.l.	b.d.l.	0.0005	0.0003	0.0001	b.d.l.	b.d.l.	0.0005	n.d.	b.d.l.	b.d.l.
Pb	b.d.l.	0.035	b.d.l.	0.004	0.010	0.011	0.018	0.005	0.003	0.006	0.004	b.d.l.	0.008	0.018	0.021
Th	b.d.l.	b.d.l.	b.d.l.	b.d.l.	b.d.l.	b.d.l.	b.d.l.	b.d.l.	b.d.l.	0.0001	b.d.l.	b.d.l.	0.0003	b.d.l.	b.d.l.
U	b.d.l.	b.d.l.	b.d.l.	b.d.l.	0.0003	0.0002	0.0002	b.d.l.	b.d.l.	0.0002	b.d.l.	0.0014	0.0001	b.d.l.	b.d.l.

In ppm or * in %. n.d.: not determined.

6.58–8.60), Zr and Hf (Zr_n/Sm_n = 4.75–22.85) anomalies and a negative Sr anomaly (Sr_n/Nd_n = 0.13–0.33).

Prograde antigorites have lower Li (0.05–0.27 ppm), B (0.6–8.5 ppm), As (0.06–0.07 ppm) and Ba (0.01–0.10 ppm) concentrations compared to lizardite and similar Sb (0.003) and Rb (≈0.07) contents. (Fig. 7 and Table 3).

In the serpentinites where all the primary phases are destabilized, the compositions and patterns of the retrograde antigorites are homogenous (Yb = 0.39–1.74 × C1-chondrite) at massif scale (Fig. 6f). They display a LREE depletion relative to M–HREE (Ce_N/Yb_N = 0.10–0.37), a weak depletion from MREE to HREE (Gd_N/Yb_N = 0.44–0.86) and a variable negative Eu anomaly (Eu/Eu* = 0.43–1.13). Extended patterns show a U-shaped pattern with positive U (U_n/Nb_n = 1.44–9.55), negative Sr (Sr_n/Nd_n = 0.10–0.39) and variable Pb anomalies (Pb_n/Ce_n = 0.48–3.90).

Retrograde antigorite FME compositions (Fig. 7 and Table 3) are similar to that of prograde antigorites (Li = 0.04–0.15 ppm, B = 0.5–4.9 ppm, As = 0.02–0.09 ppm, Sb = 0.001–0.015 ppm, Ba = 0.01–0.26 ppm, and Rb = 0.01–0.06 ppm).

4.2.4. Metamorphic veins

The chlorite and the prograde antigorite (Fig. 3c–d) show similar composition (Yb = 2.96–4.12 × C1-chondrite, Fig. 8 and Table 4) that are intermediate between clinopyroxene and orthopyroxene. They display a positive slop from LREE to HREE (Ce_N/Yb_N = 0.08–0.16) with a negative Eu anomaly (Eu/Eu* = 0.55–0.89). The extended patterns present a U-shaped pattern with a variable enrichment in alkali relative to LREE (Chlorite: Ba_n/Ce_n = 0.10–0.23, Antigorite: Ba_n/Ce_n = 0.66–2.69), negative Pb (Pb_n/Ce_n = 0.40–0.73) and Sr (Sr_n/Nd_n = 0.23–0.45) anomalies and a positive U (U_n/Nb_n = 1.38–2.51), Zr and Hf anomalies (Zr_n/Sm_n = 1.21–2.91) relative to the neighboring element.

FME content of prograde antigorite and chlorite in metamorphic veins is reported in Table 4. They have similar Li (0.18–0.39 ppm), B (5.99–6.77 ppm), As (0.08–0.09 ppm) and higher Ba (0.13–3.37 ppm), Sb (~0.02 ppm) and Rb (0.19–1.46 ppm) contents compared to the antigorite of the surrounding serpentinites.

Secondary olivines (Yb = 0.66–0.75 × C1-chondrite) have a higher trace and REE content than primary olivine (Fig. 8). They display a concave pattern with a high HREE content relative to LREE (Ce_N/Yb_N = 0.02–0.04) and MREE (Gd_N/Yb_N = 0.009–0.013). Extended patterns display positive HFSE (Zr_n/Sm_n = 20.46), Pb (Pb_n/Ce_n = 3.00–5.50) and Sr (Sr_n/Nd_n = 2.17–2.49) anomalies.

FME content of secondary olivine are reported in Table 4 and displayed in Fig. 7. They have a high Li (13.97–14.99 ppm), B (1.06–2.72 ppm) and similar As (0.07 ppm) and high Ba (0.02 ppm), Sb (<5 ppb) and Rb (<9 ppb) compared to primary olivine.

5. Discussion

Trace elements are discussed as two groups according to their behavior. The first group comprise REE and most lithophile elements. Their behavior during serpentinization processes is controlled by the initial mineralogy of the peridotite. They allow documenting the different scales of fluid circulation in the oceanic lithosphere, from the ridge to subduction. The second group (some FME: B, Li, As, Sb, Rb and Ba; and Eu) is influenced by the sequence of serpentine phase transitions during subduction, from lizardite to antigorite and then olivine. It permits to identify fluid transfers between the different envelopes composing the oceanic lithosphere and the mantle wedge and the associated changes in fluid composition during the different serpentine phase transitions.

5.1. Lizardite to antigorite phase transition

5.1.1. Trace element behavior of serpentines in slightly serpentinized peridotites

The peridotite massif of Lanzo is composed of several peridotites types (lherzolite, harzburgite, dunite, clinopyroxenite; Boudier, 1978). According to several studies (see Bodinier and Godard, 2003), the trace element composition of the peridotites is controlled by their modal composition and by the phase containing the highest trace content (clinopyroxene and orthopyroxene). Thus, before serpentinization processes, the chemical composition of the mantle section of the Lanzo massif reflected local modal heterogeneities.

The lizardite veins represent the first step of rock hydration while mesh and bastite textures result from larger water influx into the peridotite (Viti and Mellini, 1998). The trace element content of lizardite veins is similar to those of the host mineral (olivine or orthopyroxene, Fig. 6a–b). At that stage (<20% serpentinization) the trace element composition of the lizardite is inherited from the host mineral suggesting most of trace elements are immobile in the thin section scale. Mesh and bastite textures have a homogenous composition in one thin

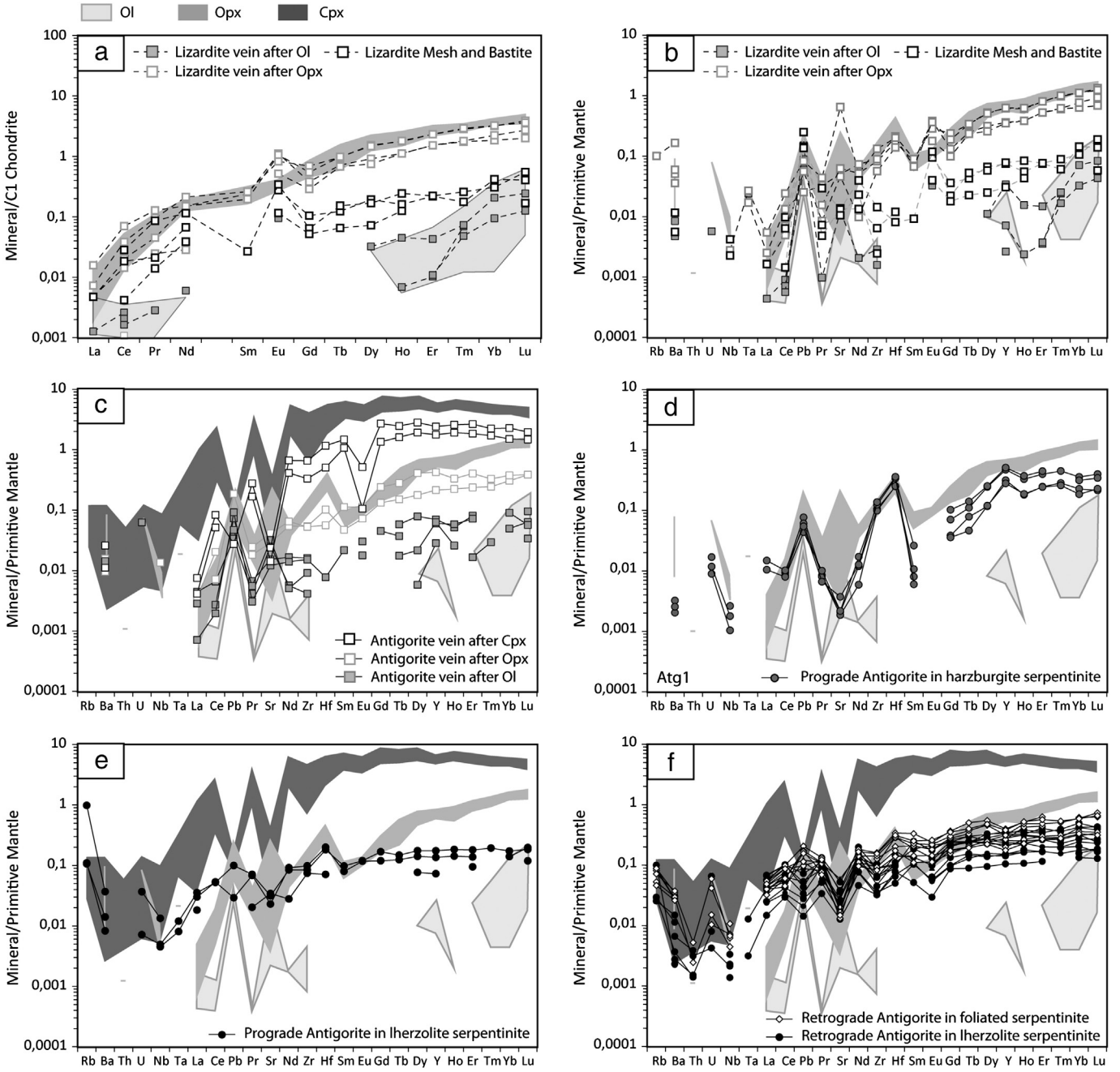

Fig. 6. Chondrite (a) and primitive mantle (b–c–d–e–f) normalized patterns for minerals composing the different lithologies of Lanzo massif. Normalizing values are from Sun and McDonough (1989). Symbols are indicated in insert. (a) REE patterns of lizardite veins crossing the Opx and the Ol and mesh and bastite texture from SSP. Host or destabilized mineral analyses are report in shaded area. (b) Spidergram of lizardite veins crossing the Opx and the Ol and mesh and bastite texture from SSP. Host or destabilized mineral analyses are report in shaded area. (c) Spidergram of prograde antigorite veins crossing the Cpx, Opx and the Ol from SSP. Host mineral analyses are reported in shaded area. (d) Spidergram of prograde antigorite from massive serpentinite Group-1. Destabilized primary minerals are report in shaded area. (e) Spidergram of prograde antigorite from massive serpentinite Group-2. Destabilized primary minerals are report in shaded area. (f) Spidergram of retrograde antigorite from FS. Destabilized primary minerals are report in shaded area.

section (Fig. 6a–b). Their composition (Yb = 0.3–0.4 × C1-chondrite) is intermediate between the olivine (Yb = 0.01–0.4 × C1-chondrite) and the orthopyroxene (Yb = 3–4 × C1-chondrite) and their patterns display a positive slope from LREE to HREE ($Ce_N/Yb_N \approx 0.01$) similar to orthopyroxene ($Ce_N/Yb_N \leq 0.01$) and olivine patterns (Ce_N/Yb_N = 0.01–0.02). The progress of the oceanic serpentinization reaction tends to homogenize the trace element content in lizardite at the thin section scale.

Even if the trace element content of oceanic lizardite is globally controlled by the destabilized primary phases, the oceanic serpentinization is marked by the occurrence of Eu (Eu/Eu^* = 1.74–7.54), Ba (Ba_n/Ce_n = 0.88–16.33), Ta (Ta_n/Ce_n = 1.11–33.67) and Sr (Sr_n/Nd_n = 0.33–12.35) positive anomalies relative to primary phases (Fig. 6a-b). The variable Sr and Ba enrichments are correlated with Ca content. Those correlations suggest that the positive Sr and Ba anomalies of lizardites result from the analysis of carbonate micro-phases during laser ablation (Deschamps et al., 2010). The development of a positive Eu anomaly during oceanic serpentinization could be attributed to the dissolution of plagioclase and/or to hydrothermal fluid circulation during lizardite formation (e.g., Douville et al., 2002; Paulick et al., 2006).

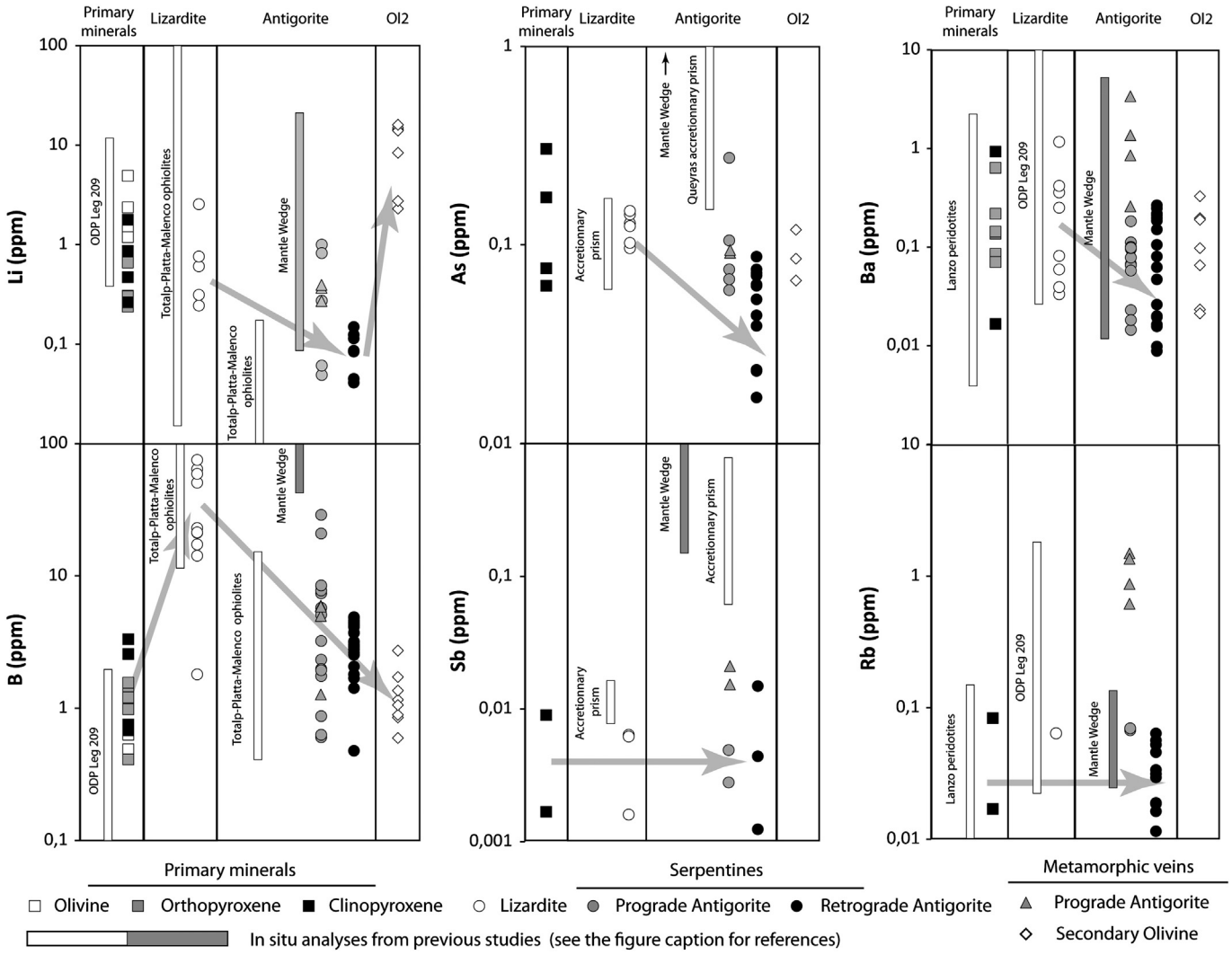

Fig. 7. Lithium (Li), Boron (B), Arsenic (As), Antimony (Sb), Rubidium (Rb) and Barium (Ba) concentration of primary minerals, serpentines and secondary olivines. The gray arrows show the chemical behaviour of those elements during the different serpentinization and de-serpentinization processes. Data from previous studies are shown for comparison: primary minerals and serpentines of abyssal peridotites from ODP Leg 209 are from Vils et al. (2008) and Andreani et al. (2009); Lizardite and antigorite of serpentinites of Totlap – Platta – Malenco ophiolites are from Vils et al. (2011); antigorite from Himalaya serpentinite are from Deschamps et al. (2010); Queyras accretionnary prism are from Lafay et al. (2013); primary minerals of Lanzo peridotites are from Piccardo et al. (2007a) and Kaczmarek and Müntener (2010).

In our samples, it is not possible to test the hypothesis of a local destabilization of plagioclase during lizardite formation since the plagioclase relicts have been replaced by high-pressure/low-temperature mineral assemblages (Debret et al., 2013). Moreover, in our samples, we are unable to correlate Sr and Eu in lizardite, which could have revealed destabilization of plagioclase, because of carbonate contamination.

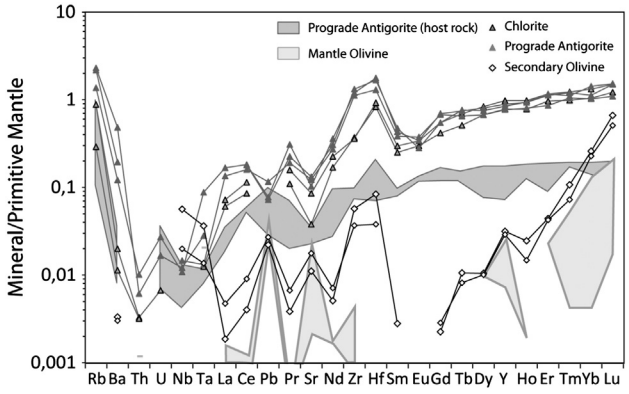

Fig. 8. In situ trace element abundances analyzed by HR-LA-ICPMS of minerals of metamorphic veins crossing the serpentinites (samples LZ34b-c) normalized to primitive mantle (Sun and McDonough, 1989).

The development of antigorite veins marks the beginning of lizardite breakdown. The antigorite veins display homogenous patterns and heterogeneous compositions. The compositions of antigorite veins ($Yb_{Atg\text{-}Ol}$ <0.3 × C1-chondrite; $Yb_{Atg\text{-}Opx}$ = 0.9–1.1 × C1-chondrite; $Yb_{Atg\text{-}Cpx}$ = 4–7 × C1-chondrite) are closed to that of the host mineral (Fig. 6c). This suggests that their composition is controlled by primary phases. However, antigorite have a flat HREE pattern (Gd_N/Yb_N = 0.43–1.18) closer to clinopyroxene (Gd_N/Yb_N = 1.08–1.45) than host minerals (Opx: Gd_N/Yb_N = 0.12–0.19, Ol: Gd << 1 ppb; Fig. 6c). This suggests that clinopyroxene destabilization is contemporaneous with antigorite crystallization. Indeed, as classically described, the clinopyroxene is resistant to low temperature oceanic serpentinization (Mével, 2003) while in alpine ophiolites, it is commonly destabilized in subduction context (e.g. Hattori and Guillot, 2007). This testifies that serpentinization is an active and continuous process from the ridge to the subduction zone. During lizardite breakdown, the water released permits the serpentinization of previously preserved phases like clinopyroxene.

Compared to lizardite, the antigorite veins formation is marked by negative Eu anomalies (Eu/Eu^* = 0.09–0.80, Fig. 6b–c). Those

Table 4
Trace element analyses (LA-ICPMS) for minerals composing the metamorphic veins.

Rock	Metamorphic veins						
Sample	LZ34c	LZ34c	LZ34c	LZ34b	LZ34b	LZ34b	LZ34b
Spot size	102	102	102	102	102	102	102
Mineral	Atg1	Atg1	Atg1	Chl	Chl	Ol2	Ol2
Li	0.367	0.393	0.270	b.d.l.	0.183	14.990	13.970
B	4.980	5.940	5.870	6.250	6.770	1.056	2.720
Si*	20.100	20.100	20.100	17.763	17.763	19.165	19.165
Ca*	0.025	0.028	0.021	0.014	0.028	b.d.l.	0.004
Sc	8.100	8.230	7.770	10.730	11.780	31.430	25.320
Ti	38.410	43.500	48.740	41.880	51.110	906.080	375.260
V	23.140	23.520	23.290	33.730	35.370	0.349	0.211
Cr*	0.000	0.000	0.000	0.006	0.004	0.000	0.000
Co	78.570	77.610	80.600	66.770	63.390	256.440	257.280
Ni*	0.154	0.158	0.148	0.160	0.155	0.290	0.301
Cu	b.d.l.	b.d.l.	0.229	b.d.l.	0.106	b.d.l.	b.d.l.
Zn	14.800	13.900	14.650	16.180	15.250	52.600	53.130
As	0.091	b.d.l.	b.d.l.	0.078	n.d.	n.d.	0.066
Rb	1.375	1.460	0.865	0.559	0.184	b.d.l.	b.d.l.
Sr	2.579	2.781	2.156	0.800	1.796	0.234	0.372
Y	3.500	3.840	4.040	3.560	4.430	0.144	0.132
Zr	12.500	14.750	13.400	4.150	4.020	0.640	0.412
Nb	0.010	0.009	0.008	b.d.l.	b.d.l.	0.040	0.014
Sb	0.015	0.021	b.d.l.	n.d.	b.d.l.	b.d.l.	b.d.l.
Cs	1.448	1.536	0.930	0.493	0.131	b.d.l.	b.d.l.
Ba	1.355	3.370	0.845	0.139	0.079	0.023	0.021
La	0.0925	n.d.	0.1148	0.0416	0.0495	0.0013	0.0033
Ce	0.2830	0.3180	0.3230	0.1512	0.2025	0.0071	0.0160
Pr	0.0526	0.0620	0.0850	0.0302	0.0435	0.0011	0.0018
Nd	0.3680	0.4140	0.4860	0.2280	0.3040	0.0069	0.0096
Sm	0.1700	0.2100	0.1910	0.1110	0.1320	0.0012	b.d.l.
Eu	0.0630	0.0470	0.0576	0.0500	0.0570	b.d.l.	b.d.l.
Gd	0.4030	0.3260	0.4140	0.2480	0.3260	0.0013	0.0017
Tb	0.0704	0.0824	0.0803	0.0551	0.0746	0.0011	0.0009
Dy	0.4950	0.5540	0.5920	0.4960	0.6150	0.0077	0.0074
Ho	0.1317	0.1538	0.1525	0.1279	0.1600	0.0040	0.0024
Er	0.4120	0.5570	0.5370	0.4620	0.5570	0.0212	0.0204
Tm	0.0774	0.0817	0.0884	0.0728	0.0905	0.0079	0.0054
Yb	0.5030	0.7000	0.5520	0.5110	0.6490	0.1273	0.1118
Lu	0.0805	0.1125	0.1106	0.0897	0.1107	0.0490	0.0375
Hf	0.400	0.517	0.545	0.256	0.285	0.026	0.012
Ta	0.0005	0.0012	0.0036	0.0005	b.d.l.	0.0015	0.0006
Pb	0.021	0.013	0.014	b.d.l.	n.d.	0.004	0.005
Th	b.d.l.	0.0005	0.0009	0.0003	0.0003	b.d.l.	b.d.l.
U	b.d.l.	0.0004	0.0006	0.0001	b.d.l.	b.d.l.	b.d.l.

In ppm or * in%.

anomalies are similar to the ones observed in the host minerals (Fig. 6c). This suggest that the Eu content of antigorite veins is inherited from the host mineral and implies that Eu is immobile at the beginning of lizardite breakdown.

5.1.2. Trace element behavior in the serpentinite units

5.1.2.1. Prograde serpentinization in massive serpentinites. Among the MS, we identified two groups based on the trace element content of whole rock analyses that can be interpreted as inherited from the SSP protolith: we distinguish serpentinites formed after lherzolites (lherzolite serpentinite) from those formed after harzburgites (harzburgite serpentinites). During the serpentinization of the MS, the trace composition of the protolith is preserved at the scale of the outcrop (~5 m) suggesting that fluid/rock interactions and trace element mobility were limited at that scale.

The MS are mostly composed of prograde and retrograde antigorite. In each MS the trace element composition of prograde antigorite is homogenous and intermediate between primary destabilized phases (Fig. 6d-e). In one harzburgite serpentinite sample, we note the occurrence of strong Zr, Hf values (Zr_n/Sm_n = 4.75–22.85) in prograde antigorite (Fig. 6e). In this sample, the microscopic observation of the primary olivine relicts does not reveal the occurrence of accessory phases but they display a low NiO and MgO content suggesting that their composition was highly modified by chemical interaction with MORB type melts (Debret et al., 2013). In this context, primary olivines are characterized by positive Zr and Hf anomalies (Drouin et al., 2009). We propose that, in this sample, the Zr and Hf anomalies of prograde antigorite are inherited.

The composition of prograde antigorite is homogenous at the outcrop scale, and its pattern is intermediate between the ones of destabilized phases. This attests that, during the transition of lizardite to antigorite, the released fluids react with minerals of the dehydrating rock at the outcrop scale. This leads to the redistribution of trace element into the newly formed antigorite and to the homogenization of its composition. Furthermore, in the massive lherzolite serpentinite, where all primary phases are destabilized, the composition and pattern of prograde antigorite are similar to those of lherzolite whole rock (Fig. 9a). This attests that, in the massive serpentinite zone of Lanzo massif, the serpentinization processes have evolved in a relative closed system for most trace elements at the scale of the outcrop from the ridge to the subduction.

5.1.2.2. Retrograde serpentinization in the serpentinites. Relative SSP and MS, the composition and pattern of whole rock trace element of FS are homogenous at the scale of the massif (Fig. 5d). They are similar to lherzolite patterns. Only few elements have a different behavior: FS display a negative anomaly in Sr (Sr_n/Nd_n = 0.08–0.99) and Eu (Eu/Eu^* = 0.09–1.07) while lherzolite display variable Sr (Sr_n/Nd_n = 0.38–1.47) and no Eu (Eu/Eu^* = 0.95–1.03) anomalies.

Locally, near the paleo-Moho, the foliation of FS surrounds lenses of MS. Next to Toglie (Fig. 1), the patterns of massive serpentinites are similar to harzburgite while the foliated serpentinites display a different

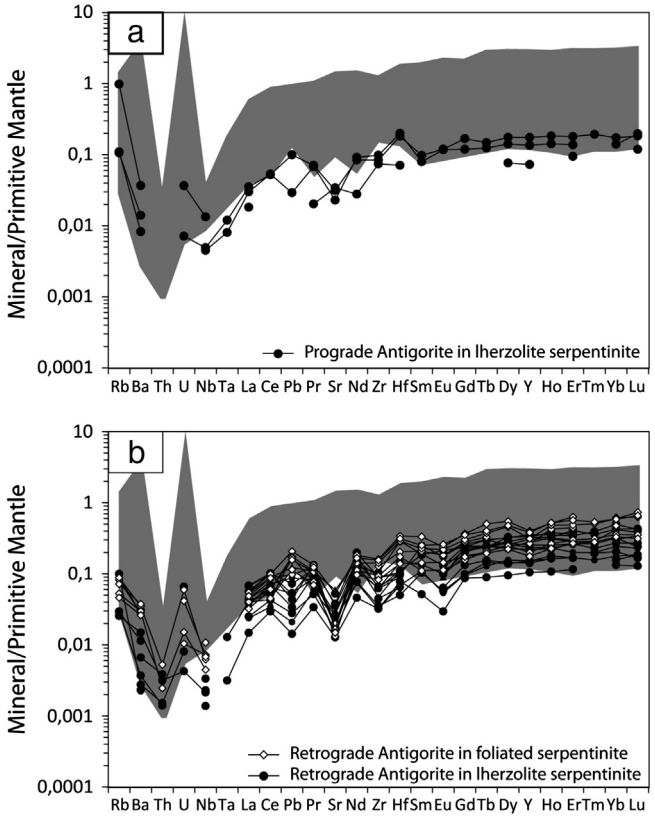

Fig. 9. Primitive mantle normalized spidergrams. Shaded area corresponds to lherzolite whole rock analyses from literature normalized to primitive mantle. (a) Spidergram of prograde antigorite from MS Group-1. (b) Spidergram of retrograde antigorite from MS Group-1 and FS.

pattern similar to lherzolite (Samples LZ26c and LZ26a: dashed line on Fig. 5c–d). If we admit that the peridotite protolith composing the outcrop was initially homogenous, this observation suggests that the composition of the FS do not depend of peridotite protolith.

In MS and FS where all primary phases are fully destabilized, the retrograde antigorite composition is homogenous and intermediate between clinopyroxene, orthopyroxene and olivine at massif scale (Fig. 6f) and its pattern is identical to the ones of the foliated serpentinite whole rock (Fig. 9b). It suggests that during retrograde serpentinization, the deformation in the FS allows a larger fluid circulation than in the rest of the massif, facilitating the mobility of trace element and permitting their redistribution within this envelop that conducts to the homogenization of antigorite composition at massif scale. The close composition of retrograde antigorite and slightly serpentinized lherzolite indicates that this recrystallization episode took place in a relative closed system.

The homogenization process of serpentine composition according to the metamorphic evolution and rock deformation is similar to the one described in Catalina Schist (Santa Catalina Island, southern California, USA). In this area, stable isotopes composition of calcschists are homogenized over significant volume of rock according to metamorphism increase (Bebout, 1991). Thus, during metamorphic processes in subduction zones, the released fluids and the deformation tend to homogenize the composition of the less competent level of the subducted lithosphere (mostly sediment and serpentinite) at large scale. This attests also for a large, kilometer-scale, fluid mobility in the less competent level of the slab.

5.1.3. FME behavior from oceanic serpentinization to lizardite breakdown into antigorite

Primary minerals in Lanzo peridotites contain 0.49–2.57 ppm of B, 0.24–4.91 ppm of Li and 0.07–0.92 ppm of Ba while the lizardite contain 1.80–75.11 ppm of B, 0.24–2.55 ppm of Li and 0.03–1.16 ppm of Ba. Those contents are similar to those observed in minerals forming abyssal and ophiolitic serpentinized peridotites (Fig. 7). The boron enrichment of lizardite, relative to primary minerals, is commonly observed in oceanic samples where it is attributed to seawater circulation during lizardite crystallization (Vils et al., 2008). This element is incorporated in serpentine structure where it saturated around 200 ppm (Pabst et al., 2011). The similar Li and Ba contents of lizardite relative to primary minerals suggest that the Li and Ba content of lizardite are controlled by primary phases (Vils et al., 2008).

During lizardite formation, we also observed the occurrence of a Eu anomaly that could be attributed to hydrothermal fluid circulation and/or to plagioclase destabilization (cf. Discussion about: 5.1.1. *Trace element behavior of serpentines in slightly serpentinized peridotites*). The petrological and trace element study do support plagioclase destabilization. However, the B contents of lizardite are correlated to their Eu content (Fig. 10a). Furthermore, relative to primary host minerals, lizardite is enriched in Eu attesting that their Eu concentration is not inherited. Consequently, it seems more likely that interaction with hydrothermal fluids, that contributed to a B enrichment in lizardite in intra oceanic context, resulted in addition of Eu. This suggests that the oceanic serpentinizing fluid leached Eu during fluid–rock interaction instead of reacting with the plagioclase of the sampled peridotite.

During prograde metamorphism in the slab, different reactions can accommodate the lizardite to antigorite transition (Oterdoom, 1978; Evans, 2004; Vils et al., 2011). In a water saturated open system, the transition lizardite to antigorite can be written as lizardite + $SiO_{2(aq)}$ → antigorite + H_2O (Coleman, 1971; Evans, 2004). In a subduction context, the required influx of SiO_2 could be generated by sediment dehydration (Deschamps et al., 2011; Lafay et al., 2013; Schwartz et al., 2013). Bebout et al. (1999) have shown that Sb and As are good markers of sediment dehydration and recent studies (Deschamps et al., 2011; Lafay et al., 2013) showed that this contamination is marked by a strong over-enrichment in Sb and As in antigorite composition (Fig. 7). In the massif of Lanzo, the Sb composition of serpentine remains unchanged from the oceanic denudation to subduction and exhumation and remains similar to that of the primitive mantle (Fig. 7). The As content varies from 0.096 to 0.148 ppm in the lizardites and to 0.017–0.086 ppm in the antigorites. Those values are lower than those of antigorite from sediment/serpentinite systems (e.g. Queyras, Lafay et al., 2013); suggesting that the Lanzo massif was not contaminated by sediment-derived fluids during subduction. Furthermore, in opposition to the accretionnary prism of the Queyras where serpentine As content increases during the transition lizardite to antigorite (Lafay et al., 2013), the content of As in lizardite of the Lanzo massif decreases with antigorite crystallization. Thus, it rather suggests that As would be released from the slab in a fluid phase during prograde metamorphism. This is in good agreement with Izu Bonin arc studies where few sediments are involved in the subduction and where mantle wedge serpentinites display high As content relative to abyssal serpentinites (Savov et al., 2005, 2007). Thus, the fluid released during the lizardite/antigorite phase transition could also generate this type of enrichment in mantle wedge serpentinites.

Prograde and retrograde antigorite display a similar B, Li and Ba content in MS and in the FS. They contain up to 0.48–8.46 ppm of B, 0.04–1.00 ppm of Li and <0.01–0.26 ppm of Ba. Those values are lower than the ones of lizardite. As previously observed by Vils et al. (2011), the lizardite to antigorite transition leads to a loss of Li, B and Ba. This is also in agreement with the fact that B is incorporated in serpentine structure (Pabst et al., 2011), and can be released during the dissolution–recrystallization of lizardite to antigorite. Due to the high solubility of Li, B and Ba in fluids, these results suggest that these elements should be enriched in the fluids that were released from the system.

In contrast to the oceanic serpentinization, in SSP, Eu is immobile during the first stage of lizardite breakdown into antigorite (cf. Discussion about: 5.1.1. *Trace element behavior of serpentines in slightly serpentinized peridotites*). In MS and FS, antigorite display no or negative Eu anomalies relative to neighboring elements (Fig. 6). In those rocks, the Eu content of antigorite is correlated with the B content diminution (Fig. 9b). This suggests that Eu have a similar behavior as B and is released by fluid during lizardite breakdown. The Eu complexiation and mobility is controlled by the chlorinity, the pH or the redox potential of the fluid (Savov et al., 2005; Paulick et al., 2006; Savov et al., 2007).

Evans (2004) proposed the H_2O-conserved reaction: Liz → Atg + Brc. Nevertheless, in the studied samples, there is no brucite associated with antigorite (Debret et al., 2013). Furthemore, our results provide evidence of loss of several FME (As, Li, B and Ba) and Eu during lizardite to antigorite transition. Those elements are highly mobile in fluids suggesting that they are expulsed from the subducted lithosphere in a fluid phase. Hence a conserved reaction for these elements cannot be considered in the Lanzo massif. As previously demonstrated there are no inlet fluid during subduction, thus the lizardite to antigorite transition should be written this way: lizardite → antigorite + $MgO_{(aq)}$ + H_2O, rather than with addition of silica lizardite + $SiO_{2(aq)}$ → antigorite + H_2O.

Prograde transition lizardite to antigorite is expected to contribute to the FME enrichment of mantle wedge peridotite and serpentinite (Hattori and Guillot, 2007). The compositions and patterns of mantle wedge antigorite display similar B, Li and Ba contents and higher As and Sb content (Deschamps et al., 2010) than those reported from oceanic context (Vils et al., 2008; Andreani et al., 2009, Fig. 6). Their patterns do not display negative Eu anomaly (Deschamps et al., 2010). Our results show that the fluid released during lizardite breakdown carry B, Li, Ba, As and Eu. That fluid could contribute to form FME rich antigorite in the mantle wedge peridotite. Arc magmas and their primary melt inclusions are also enriched in some FME (e.g. B, Li, As) relative to MORB or OIB suggesting that those elements are transferred from the slab to the arc magma source in deep mantle (Ryan et al., 1995; Noll et al., 1996). Nevertheless, those elements seem to be mostly released from slab serpentinites in the first 70 km of subduction into the serpentinized mantle wedge and thus before peridotite melting. As it was first proposed by Savov et al. (2007), this observation suggests

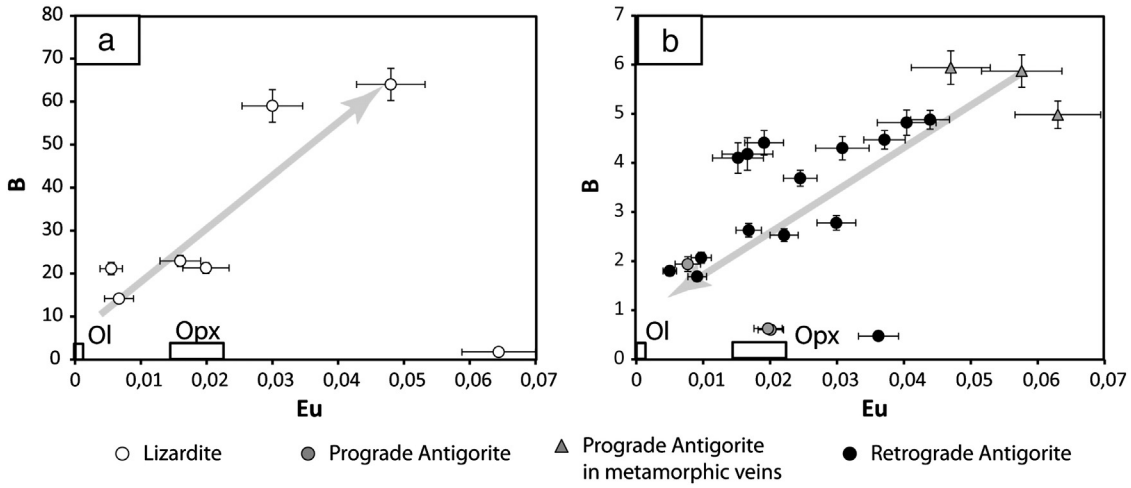

Fig. 10. (a) Plot of Eu versus B of lizardite of SSP. (b) Plot of Eu versus B of antigorite and secondary olivine composing the serpentinites (MS, FS and metamorphic veins) of Lanzo massif.

that mantle wedge serpentinites have to be dragged down to the deep mantle in order to participate to arc magma chemistry.

5.2. Metamorphic veins

The massive ultramafic rocks (SSP and MS) of Lanzo massif display an interconnected network of metamorphic veins containing high pressure assemblages (Fig. 3). The preferential crystallization of secondary olivine in those veins, relative to the host rocks, attests that those veins localized the fluid release and behaved as high permeability reaction zones (Gao and Klemd, 2001; John et al., 2007).

5.2.1. Behavior of trace element during the lizardite breakdown to antigorite and secondary olivine

The trace element compositions of the prograde antigorite/chlorite (Fig. 8) are identical suggesting that these minerals crystallized after the same mineralogical assemblages. They display positive Zr and Hf (Zr_n/Sm_n = 1.21–2.91) anomalies and a HREE enrichment relative to MREE (Gd_N/Yb_N = 0.39–0.66). The fractionation of HFSE and HREE indicates a fluid release during the formation of prograde antigorite (Garrido et al., 2005).

When the composition of the lherzolite is used as a reference value for normalizing trace element concentrations (Fig. 11), the variation of trace element content between antigorite in metamorphic veins, and antigorite in host rock, suggests that veins had a different behavior from host rock during fluid rock interactions. On Fig. 11, the prograde and retrograde antigorite trace element concentration is inferior to 1. This suggests a dilution of trace element resulting from the volume increased during serpentinization process (Mével, 2003). These lherzolite-normalized patterns also show a flat pattern from LREE to HREE, confirming that their formation is globally isochemical.

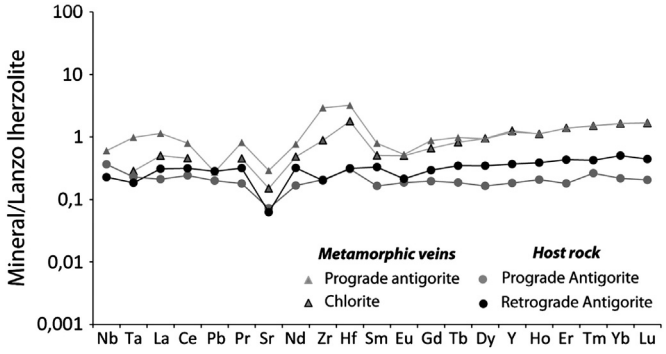

Fig. 11. Mean value of trace elements of the prograde and retrograde antigorites and chlorite of the metamorphic veins and serpentinite host rocks normalized to the composition of the slightly serpentinized lherzolite. The prograde and retrograde antigorites of the host rock do no show fractionations of trace elements relative to the initial protholite composition during the successive serpentinization steps occurring from the ridge to the subduction. The prograde antigorite/chlorite of the metamorphic veins fractionate HREE and HFSE demonstrating a different behaviour during serpentinization processes.

Small amounts of water can transport trace elements from the host rock to high permeability veins without significantly changing the host rock element budget (Liebscher, 2004). The fluid flow within the veins will create locally higher fluid rock ratio allowing the transport of trace element to long distance, until they eventually exit the massive compartments (SSP and MS). The prograde antigorites composing the metamorphic veins probably crystallized after the enriched fluid circulating within the high permeability veins, thus explaining their trace element enrichments.

Relative to primary olivine (Yb = 0.01–0.4 × C1-chondrite, Nb << 1 ppb, Ta_n = 0.02, $Zr_n \leq 0.004$, Hf << 1 ppb), the secondary olivines are enriched in HREE (Yb = 0.66–0.75 × C1-chondrite) and HFSE (Nb_n = 0.02–0.06, Ta_n = 0.01–0.04, Zr_n = 0.04–0.06, Hf_n = 0.04–0.06, Fig. 8 and Table 4). These HREE and HFSE positive anomalies relative to elements of similar compatibility have already been observed in secondary olivine from Cerro Del Almirez massif (Garrido et al., 2005). It suggests that those anomalies could be typical of secondary olivine crystallization.

In contrast to the lizardite to antigorite transition, the antigorite to olivine transition releases a great quantity of water (Scambelluri et al., 2004). The lower trace element contents of secondary olivine relative to prograde antigorite require high water/rock ratio to transport trace elements away from the dehydrating zones (John et al., 2007), implying that the formation of the metamorphic veins by dehydration occurred in an open system. The high fractionation of HFSE, HREE and Sr, relative to element of similar compatibility, indicates that the out coming fluid in equilibrium with metamorphic veins is depleted in HFSE, HREE and Sr relative to L-MREE. The immobility of HFSE and HREE has already been observed in subduction zones (Garrido et al., 2005; Savov et al., 2005, 2007). These elements are not released in the fluid during slab dehydration and will stay in the slab at greater depth.

5.2.2. Behavior of FME in the metamorphic veins

Antigorite and olivine from metamorphic veins are respectively enriched in Rb and B, or Li relative to antigorite from SSP, MS and FS (Fig. 7). This relative enrichment of LILE in transport veins has already been observed in eclogitic veins (John et al., 2007) where it is interpreted as carried by the external fluid circulation. Indeed, the

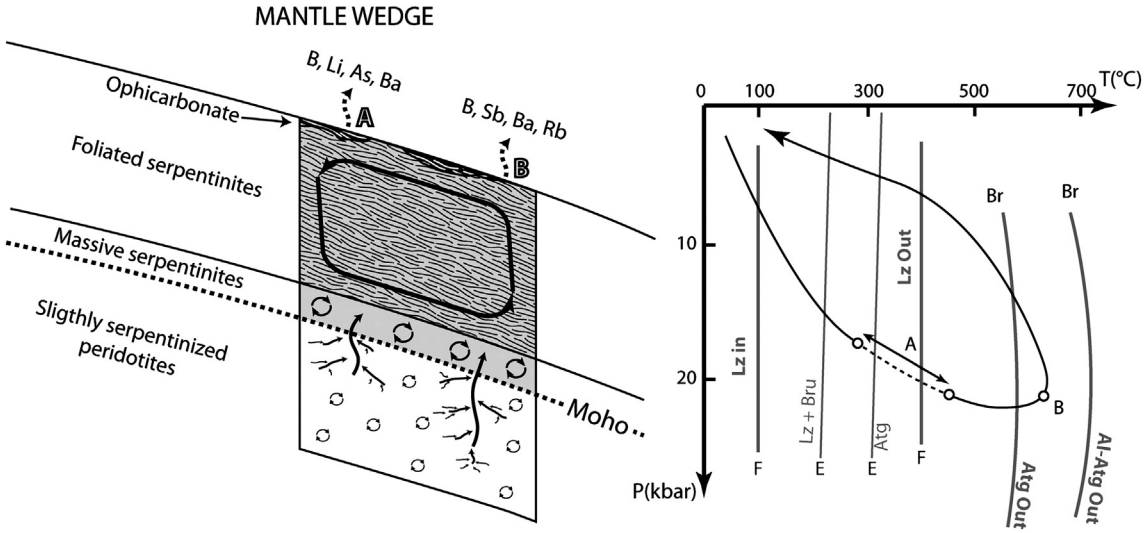

Fig. 12. Conceptual model illustrating the fluid circulation in the oceanic lithosphere during subduction. In the serpentinite part of the lithosphere, the high alpine deformation allows a fluid circulation – and trace element mobility – at massif scale (black arrow, the arrow size indicates the scale of fluid fluxes). In the massive part, the fluid circulation is limited at the outcrop scale; the exchange between the different ultrabasic envelopes is limited to transport veins crossing the massive rocks (arrow). In those veins the fluid released is depleted in HFSE and HREE. During the different phase transitions of the serpentine (A and B), the FME are continuously released by fluid. This suggests that FME are able to be transport by fluid trough the different ultrabasic envelopes of the lithosphere to the mantle wedge (dashed arrows). Reported reactions are from: F: Martin and Fyfe, 1970; E: Evans, 2004; Br: Bromiley and Pawley, 2003.

fluid circulating into the metamorphic veins mainly mobilizes LREE and LILE relative to HREE and HFSE. The newly formed minerals are able to scavenge the FME during their crystallization.

Relative to prograde antigorite composing the metamorphic veins, the secondary olivines display lower B, Sb and Rb (Fig. 7). This confirms that B is also removed during antigorite breakdown and is good tracer of serpentine dehydration in subduction zones (Scambelluri and Tonarini, 2012). The Sr and Rb are released at deep levels of subduction, only during the antigorite breakdown, by fluids and possibly transported to the mantle wedge.

6. Conclusions

During subduction, the oceanic structure is preserved, at the Moho the peridotites are poorly serpentinized (<20% serpentinization) while the upper part of the lithosphere is mainly made up of serpentinite. The most serpentinized part of the oceanic lithosphere (>20% serpentinization) accommodates preferentially the deformation during subduction and exhumation history. This favors fluid circulation and its complete recrystallization in antigorite while the peridotite is poorly deformed and preserves the oceanic serpentinization.

In the upper part of oceanic lithosphere, the deformation and the high fluid circulation enhances the mobility of trace element and permits their redistribution and the homogenization of antigorite composition at massif scale (Fig. 12). The successive crystallization of lizardite and antigorite do not fractionate the lherzolite trace element composition indicating that the serpentinization is a homogenization process globally isochemical (Fig. 11). At the Moho and in the lower part of the lithosphere, the low fluid/rock ratio does not permit high trace element mobility and the redistribution of trace element is limited at the outcrop scale. However, locally, the observation of metamorphic veins, containing high pressure assemblages (prograde antigorite/chlorite and secondary olivine) that highly fractionate HFSE and HREE relative to serpentine of the host rock (Fig. 11), attests that those fluid flow channels are able to transport trace element to long distance. The transport of fluid — and thereby of trace element — into these fluid flow channels suggests that the lower part of the oceanic lithosphere can contribute to the water recycling of subduction zone.

Our results show evidences of loss of FME and Eu during lizardite to antigorite and then antigorite to secondary olivine phase transitions. The good complementarity of these results with previous works realized on mantle wedge serpentine (Savov et al., 2005, 2007; Deschamps et al., 2010) strongly suggests that those elements are continuously removed from the slab to the mantle wedge during the devolatilisation of the oceanic lithosphere in subduction context.

Supplementary data to this article can be found online at http://dx.doi.org/10.1016/j.chemgeo.2013.08.025.

Acknowledgments

This study is a Laboratory of excellence *ClerVolc* contribution n°71. It was supported by INSU Systerre and Labex@2020. S. Guillot (ISTerre, Grenoble), O. Laurent (Magmas et Volcans, Clermont-Ferrand) and F. Deschamps (Geosciences, Montpellier) are thanked for fruitful discussions. We also acknowledge C. Constantin (Magmas et Volcans, Clermont-Ferrand) for thin section preparations, M. Benbakkar (Magmas et Volcans, Clermont-Ferrand) and O. Bruguier (Geosciences, Montpellier) for their assistance during ICP-AES and LA-ICPMS analyses. We thank an anonymous reviewer for critical comments on earlier version of this article and careful editorial handling by D. Dingwell.

References

Agrinier, P., Cannat, M., 1997. Oxygen isotopic constraints on serpentinization processes in ultramafic rocks from the Mid-Atlantic Ridge (23°N) in the MARK area. In: Karson, J.A., Cannat, M., Miller, D.J., Elthon, D. (Eds.), Proceedings of the Ocean Drilling Program. Scientific Results, 153, pp. 381–388.

Andreani, M., Mével, C., Boullier, A.-M., Escartin, J., 2007. Dynamic control on serpentine crystallization in veins: constraints on hydration processes in oceanic peridotites. Geochem. Geophys. Geosyst. 8, Q02012. http://dx.doi.org/10.1029/2006GC001373.

Andreani, M., Godard, M., Mével, C., 2009. LA-(HR-)ICPMS study of serpentinites from ODP Site 920 (23°N MAR): insights on transfers and trace element distribution during serpentinization. Geophys. Res. EGU2009 (Abstracts no. 13248).

Bach, W., Garrido, C.J., Paulick, H., Harvey, J., Rosner, M., 2004. Seawater-peridotite interactions: first insights from ODP Leg 209, MAR 15 N. Geochem. Geophys. Geosyst. 5, Q09F26. http://dx.doi.org/10.1029/2004GC000744.

Bebout, G.E., 1991. Field-based evidence for devolatilization in subduction zones: implications for arc magmatism. Science 251, 413–416.

Bebout, G.E., Ryan, J.G., Leeman, W.P., Bebout, A.E., 1999. Fractionation of trace elements by subduction-zone metamorphism — effect of convergent-margin thermal evolution. Earth Planet. Sci. Lett. 171, 63–81.

Bodinier, J.L., 1988. Geochemistry and petrogenesis of the Lanzo peridotite body, Western Alps. Tectonophysics 149, 67–88.

Bodinier, J.L., Godard, M., 2003. In: Carlson, R.W. (Ed.), Orogenic, Ophiolitic, and Abyssal Peridotites. Treatise on Geochemistry, vol. 2. Mantle and Core, Elsevier Science Ltd, pp. 103–170.

Boudier, F., 1978. Structure and petrology of the Lanzo peridotite massif (Piedmont Alps). Geol. Soc. Am. Bull. 89, 1574–1591.

Bromiley, G.D., Pawley, A.R., 2003. The stability of antigorite in the systems MgO–SiO_2–H_2O (MSH) and MgO–Al_2O_3–SiO_2–H_2O (MASH): the effects of Al_3+ substitution on high-pressure stability. Am. Mineral. 88, 99–108.

Canales, J.P., Collins, J.A., Escartin, J., Detrick, R.S., 2000. Seismic structure across the rift valley of the Mid-Atlantic ridge at 23°20′N (MARK area): implications for crustal accretion processes at slow-spreading ridges. J. Geophys. Res. 105, 28411–28425.

Cannat, M., Mével, C., Maïa, M.M., Deplus, C., Gente, P., Agrinier, P., Belarouchi, A., Dubuisson, G., Humler, E., Reynolds, J.R., 1995. Thin crust, ultramafic exposure and rugged faulting patterns at the Mid- Atlantic Ridge (22°–24′N). Geology 23, 49–52.

Coleman, R.G., 1971. Petrologic and geophysical nature of serpentinization. Geol. Soc. Am. Bull. 82, 918–987.

Debret, B., Nicollet, C., Andreani, M., Schwartz, S., Godard, M., 2013. Three steps of serpentinization in an eclogitized oceanic serpentinization front (Lanzo Massif – Western Alps). J. Metamorph. Geol. 31, 165–186.

Deschamps, F., Guillot, S., Godard, M., Chauvel, C., Andreani, M., Hattori, K., 2010. In situ characterization of serpentinites from forearc mantle wedges: timing of serpentinization and behavior of fluid–mobile elements in subduction zones. Chem. Geol. 269, 262–277.

Deschamps, F., Guillot, S., Godard, M., Andreani, M., Hattori, K., 2011. Serpentinites act as sponges for fluid–mobile-elements in abyssal and subduction zone environments. Terra Nova 23, 171–178.

Dick, H.J.B., Lin, J., Schouten, H., 2003. An ultraslow–spreading class of ocean ridge. Nature 426, 405–412.

Douville, E., Charlou, J.L., Oelkers, E.H., Bienvenu, P., Jove Colon, C.F., Donval, J.P., Fouquet, Y., Pricur, D., Appriou, P., 2002. The Rainbow vent fluids (36°14′N, MAR): the influence of ultramafic rocks and phase separation on trace element content in mid-atlantic ridge hydrothermal fluids. Chem. Geol. 184, 37–48.

Drouin, M., Godard, M., Ildefonse, B., Bruguier, O., Garrido, C.J., 2009. Geochemical and petrographic evidence for magmatic impregnation in the oceanic lithosphere at Atlantis Massif, Mid-Atlantic Ridge (IODP Hole U1309D, 30_N). Chem. Geol. 264, 71–88.

Evans, B., 2004. The serpentinite multisystem revisited: Chrysotile is metastable. Int. Geol. Rev. 46, 479–506.

Gao, J., Klemd, R., 2001. Primary fluids entrapped at blueschist to eclogite transition; evidence from the Tianshan meta-subduction complex in northwestern China. Contrib. Mineral. Petrol. 142, 1–14.

Garrido, C.J., Lopez Sanchez-Vizcaino, V., Gomez-Pugnaire, M.T., Trommsdorff, V., Alard, O., Bodinier, J.L., Godard, M., 2005. Enrichment of HFSE in chlorite–harzburgite produced by high-pressure dehydration of antigorite–serpentinite: implications for subduction magmatism. Geochem. Geophys. Geosyst. 6, Q01J15. http://dx.doi.org/10.1029/2004GC000791.

Godard, M., Jousselin, D., Bodinier, J.-L., 2000. Relationships between geochemistry and structure beneath a palaeo-spreading centre: a study of the mantle section in the Oman Ophiolite. Earth Planet. Sci. Lett. 180, 133–148.

Godard, M., Lagabrielle, Y., Alard, O., Harvey, J., 2008. Geochemistry of the highly depleted peridotites drilled at ODP Sites 1272 and 1274 (Fifteen-Twenty Fracture Zone, Mid-Atlantic Ridge): implications for mantle dynamics beneath a slow spreading ridge. Earth Planet. Sci. Lett. 267, 410–425.

Govindaraju, K., 1994. Compilation of working values and sample description for 383 geostandards. Geostand. Newslett. 18, 1–158.

Groppo, C., Compagnoni, C., 2007. Metamorphic veins from the serpentinites of the Piemonte Zone, western Alps, Italy: a review. Periodico di Mineralogica 76, 127–153.

Gunther, D., Heinrich, C., 1999. Enhanced sensitivity in laser ablation-ICP mass spectrometry using heliu–argon mixtures as aerosol carrier. J. Anal. At. Spectrom. 14, 1363–1368.

Hattori, K., Guillot, S., 2007. Geochemical character of serpentinites associated with high to ultrahigh-pressure metamorphic rocks in the Alps, Cuba, and the Himalayas: recycling of elements in subduction zones. Geochem. Geophys. Geosyst. 8, Q09010. http://dx.doi.org/10.1029/2007GC001594.

Ionov, D.A., Savoyant, L., Dupuy, C., 1992. Application of the ICP-MS technique to trace element analysis of peridotites and their minerals. Geostand. Newslett. 16, 311–315.

Jochum, K.P., Seufert, H.M., Thirwall, M.F., 1990. High-sensitivity Nb analysis by spark-source mass spectrometry (SSMS) and calibration of XRF Nb and Zr. Chem. Geol. 81, 1–16.

John, T., Klemd, R., Gao, J., Garbe-Schonberg, C.D., 2007. Trace-element mobilization in slabs due to non steady-state fluid–rock interaction: constraints from an eclogite-facies transport vein in blueschist (Tianshan, China). Lithos 103, 1–24.

Kaczmarek, M.A., Müntener, O., 2008. Juxtaposition of melt impregnation and high-temperature shear zones in the upper mantle; Field and petrological constraints from the Lanzo Peridotite (Northern Italy). J. Petrol. 49, 2187–2220.

Kaczmarek, M.A., Müntener, O., 2010. The variability of peridotite composition across a mantle shear zone (Lanzo massif, Italy): interplay of melt focusing and deformation. Contrib. Mineral. Petrol. 160, 663–679.

Kodolanyi, J., Pettke, T., 2011. Loss of trace elements from serpentinites during fluid-assisted transformation of chrysotile to antigorite — an example from Guatemala. Chem. Geol. 284, 351–362.

Kodolanyi, J., Pettke, T., Spandler, C., Kamber, B.S., Gméling, K., 2012. Geochemistry of ocean floor and fore-arc serpentinites: constraints on the ultramafic input to subduction zones. J. Petrol. 53, 235–270.

Lafay, R., Deschamps, F., Schwartz, S., Guillot, S., Godard, M., Debret, B., Nicollet, C., 2013. High-pressure serpentinites, a trap-and-1 release system controlled by metamorphic conditions: example from the Piedmont zone of the western Alps. Chem. Geol. 343, 38–54.

Lagabrielle, Y., Fudural, S., Kienast, J.R., 1989. La couverture océanique des ultrabasites de Lanzo (Alpes occidentales): arguments lithostratigraphiques et pétrologiques. Geodin. Acta 3, 43–55.

Liebscher, A., 2004. Decoupling of fluid and trace element release in subducting slab? Comment on redistribution of trace elements during prograde metamorphism from lawsonite blueschist to eclogite facies; implications for deep subduction-zone processes by C. Spandler et al. (2003). Contrib. Mineral. Petrol. 148, 502–505.

Martin, B., Fyfe, W.S., 1970. Some experimental and theoretical observations on the kinetics of hydration reactions with particular reference to serpentinisation. Chem. Geol. 6, 185–202.

Mével, C., 2003. Serpentinization of abyssal peridotites at mid-ocean ridges. C. R. Geosci. 335, 825–852.

Morishita, T., Hara, K., Nakamura, K., Sawaguchi, T., Tamura, A., Arai, S., Okino, K., Takai, K., Kumagai, H., 2009. Igneous, alteration and exhumation processes recorded in abyssal peridotites and related fault rocks from an Oceanic Core Complex along the Central Indian Ridge. J. Petrol. 50, 1299–1325.

Müntener, O., Piccardo, G.B., Polino, R., Zanetti, A., 2005. Revisiting the Lanzo peridotite (NW-Italy): "asthenospherization" of ancient mantle lithosphere. Ofioliti 30, 111–124.

Nicolas, A., Bouchez, J.L., Boudier, F., 1972. Interprétation cinématique des déformations plastiques dans le massif de lherzolite de Lanzo (Alpes piemontaises) — comparaison avec d'autres massifs. Tectonophysics 14, 143–171.

Noll Jr., P.D., Newsom, H.E., Leeman, W.P., Ryan, J.G., 1996. The role of hydrothermal fluids in the production of subduction zone magmas: evidence from siderophile and chalcophile trace elements and boron. Geochim. Cosmochim. Acta 60, 587–611.

Oterdoom, W.H., 1978. Tremolite- and diopside-bearing serpentine assemblages in the CaO–MgO–SiO_2–H_2O multisystem. Schweiz. Mineral. Petrogr. Mitt. 58, 127–138.

Pabst, S., Zack, T., Savov, I.P., Ludwig, T., Rost, D., Vicenzi, E.P., 2011. Evidence for boron incorporation into the serpentine crystal structure. Am. Mineral. 96, 1112–1119.

Padron-Navarta, J.A., Hermann, J., Garrido, C.J., Sanchez-Vizcaino, V.L., Gomez-Pugnaire, M.T., 2010. An experimental investigation of antigorite dehydration in natural silica-enriched serpentinite. Contrib. Mineral. Petrol. 159, 25–42.

Paulick, H., Bach, W., Godard, M., De Hoog, J.C.M., Suhr, G., Harvey, J., 2006. Geochemistry of abyssal peridotites (Mid-Atlantic Ridge, 15°20′N, ODP Leg 209): implications for fluid/rock interaction in slow spreading environments. Chem. Geol. 234, 179–210.

Pearce, N.J.G., Perkins, W.T., Westgate, J.A., Gorton, M.P., Jackson, S.E., Neal, C.R., Chenery, S.P., 1997. A compilation of new and published major and trace element data for NIST SRM 610 and NIST SRM 612 glass reference materials. Geostandards Newsletter 21, 115–144.

Pelletier, L., Müntener, O., 2006. High-pressure metamorphism of the Lanzo peridotite and its oceanic cover, and some consequences for the Sezia–Lanzo zone (northwestern Italian Alps). Lithos 90, 111–130.

Piccardo, G.B., Zanetti, A., Pruzzo, A., Padovano, M., 2007a. The North Lanzo peridotite body (NW Italy): lithospheric mantle percolated by MORB and alkaline melts. Period. Mineral. 76, 199–221.

Piccardo, G.B., Zanetti, A., Müntener, O., 2007b. Melt/peridotite interaction in the Southern Lanzo peridotite: field, textural and geochemical evidence. Lithos 94, 181–209.

Ryan, J.G., Morris, J., Tera, F., Leeman, W.P., Tsvetkov, A., 1995. Cross-arc geochemical variations in the Kurile arc as a function of slab depth. Science 270, 625–627.

Savov, I.P., Ryan, J.G., D'Antonio, M., Kelley, K., Mattie, P., 2005. Geochemistry of serpentinized peridotites from the Mariana Forearc–Conical Seamount, ODP Leg 125: Implications for the elemental recycling at subduction zones. Geochem. Geophys. Geosyst. 6, Q04J15. http://dx.doi.org/10.1029/2004GC000777.

Savov, I.P., Ryan, J.G., D'Antonio, M., Fryer, P., 2007. Shallow slab fluid release across and along the Mariana arc-basin system: Insights from geochemistry of serpentinized peridotites from the Mariana fore arc. J. Geophys. Res. 112. http://dx.doi.org/10.1029/2006JB004749.

Scambelluri, M., Tonarini, S., 2012. Boron isotope evidence for shallow fluid transfer across subduction zones by serpentinized mantle. Geology 40, 907–910.

Scambelluri, M., Bottazzi, P., Trommsdorff, V., Vannucci, R., Hermann, J., Gomez-Pugnaire, M.T., Lopez-Sanchez Vizcaino, V., 2001. Incompatible element-rich fluids released by antigorite breakdown in deeply subducted mantle. Earth Planet. Sci. Lett. 192, 457–470.

Scambelluri, M., Fiebig, J., Malaspina, N., Müntener, O., Pettke, T., 2004. Serpentinite subduction: implications for fluid processes and trace-element recycling. Int. Geol. Rev. 46, 595–613.

Schwartz, S., Guillot, S., Reynard, B., Lafay, R., Debret, B., Nicollet, C., Lanari, P., Auzende, A.L., 2013. Pressure–temperature estimates of the lizardite/antigorite transition in high pressure serpentinites. Lithos. http://dx.doi.org/10.1016/j.lithos.2012.11.02.

Sun, S., McDonough, W.F., 1989. Chemical and Isotopic Systematics of Oceanic Basalts: Implications for Mantle Composition and Processes. In: Saunders, A.D., Norry, M.J. (Eds.), Magmatism in the ocean basins. Geological Society Special Publication, 42, pp. 313–345.

Van Achterberg, E., Ryan, C., Jackson, S., Griffin, W., 2001. Data Reduction Software for LA-ICP-MS. In: Sylvester, P. (Ed.), Laser ablation ICP-MS in the Earth Science. Mineralogical Association of Canada, pp. 239–243.

Vils, F., Pelletier, L., Kalt, A., Müntener, O., Ludwig, T., 2008. The lithium, boron and beryllium content of serpentinized peridotites from ODP Leg 209 (Sites 1272A and 1274A): implications for lithium and boron budgets of oceanic lithosphere. Geochim. Cosmochim. Acta 72, 5475–5504.

Vils, F., Müntener, O., Kalt, A., Ludwig, T., 2011. Implications of the serpentine phase transition on the behaviour of beryllium and lithium-boron of subducted ultramafic rocks. Geochim. Cosmochim. Acta 75, 1249–1271.

Viti, C., Mellini, M., 1998. Mesh textures and bastites in the Elba retrograde serpentinites. Eur. J. Mineral. 10, 1341–1359.

Whitney, D.L., Evans, B.W., 2010. Abbreviations for names of rock-forming minerals. Am. Mineral. 95, 185–187.

Wunder, B., Schreyer, W., 1997. Antigorite: high-pressure stability in the system MgO–SiO_2–H_2O (MSH). Lithos 41, 213–227.